Correlated nanoscale characterization of a unique complex oxygen-rich stardust grain: Implications for circumstellar dust formation

J. Leitner [a],*, P. Hoppe [a], C. Floss [b], F. Hillion [c], T. Henkel [d]

[a] *Max Planck Institute for Chemistry, Particle Chemistry Department, Hahn-Meitner-Weg 1, 55128 Mainz, Germany*
[b] *Laboratory for Space Sciences and Physics Department, Washington University, One Brookings Drive, St. Louis, MO 63130, USA*
[c] *Cameca, Gennevilliers, France*
[d] *The University of Manchester, School of Earth and Environmental Sciences, Williamson Building, Oxford Road, Manchester M13 9PL, UK*

Abstract

We report the light to intermediate-mass element abundances as well as the oxygen, magnesium, silicon, and titanium isotope compositions of a unique and unusually large (0.8 μm × 3.75 μm) presolar O-rich grain from the Krymka LL3.2 chondrite. The O-, Al-, and Ti-isotopic compositions are largely compatible with an origin from an asymptotic giant branch (AGB) star of 1.5 solar masses with a metallicity that is 15% higher than the solar metallicity. The grain has an elevated $^{17}O/^{16}O$ ratio $(8.40 \pm 0.16 \times 10^{-4})$ compared to solar, and slightly sub-solar $^{18}O/^{16}O$ ratio $(1.83 \pm 0.03 \times 10^{-3})$. It shows evidence for the presence of initial ^{26}Al, suggesting formation after the first dredge-up, during one of the early third dredge-up (TDU) episodes. Titanium isotopic data indicate condensation of the grain before significant amounts of material from the He-burning shell were admixed to the stellar surface with progressive TDUs. We observed a small excess in ^{30}Si ($\delta^{30}Si = 41 \pm 5‰$), which most likely is inherited from the parent star's initial Si-isotopic composition. For such stars stellar models predict a C/O-ratio < 1 even after the onset of TDU, thus allowing the condensation of O-rich dust.

The grain is an unusual complex presolar grain, consisting of an Al-Ca-Ti-oxide core, surrounded by an Mg-Ca-silicate mantle, and resembles the condensation sequence for a cooling gas of solar composition at pressures and dust/gas ratios typically observed for circumstellar envelopes around evolved stars. We also report the first observation of phosphorus in a presolar grain, although the origin of the P-bearing phase remains ambiguous.
© 2017 Elsevier Ltd. All rights reserved.

1. INTRODUCTION

Refractory dust grains with highly anomalous isotopic compositions, so-called "presolar" or "stardust" grains, are found in small quantities in primitive Solar System materials such as unequilibrated meteorites, interplanetary dust particles (IDPs), and cometary dust (Zinner, 2014).

The isotopic anomalies cannot be explained by chemical or physical Solar System processes, but require nucleosynthetic reactions in stellar environments. These stardust grains condensed in the winds of evolved stars and in the ejecta of stellar explosions and carry the isotopic fingerprints of their parent stars. During their passage through the interstellar medium (ISM), they were exposed to shockwaves from nearby supernova explosions, grain-grain-collisions, and high-energetic irradiation (e.g., Woitke et al., 1993; Jones et al., 1996; Dwek, 1998).

---

* Corresponding author.
  E-mail address: jan.leitner@mpic.de (J. Leitner).

Subsequently, stardust grains were incorporated into the gas and dust cloud from which our Solar System formed, and a fraction of them survived equilibration and alteration processes during the various Solar System formation stages (e.g., Cameron, 1962, 1973; Lodders and Amari, 2005; Zinner, 2014). The study of the isotopic compositions of these grains, as well as their elemental compositions and mineralogy, provides valuable information on stellar nucleosynthesis and evolution, grain growth in circumstellar environments, the types of stars that contributed material to the molecular cloud from which our Solar System formed, and chemical and physical processes in the ISM and in the Solar System.

With the exception of nanodiamonds, whose origins are still a matter of debate, silicates are the most abundant type of presolar grain (e.g., Zinner, 2014). Primitive IDPs contain ∼400 ppm (ppm) on average (Floss et al., 2006), with abundances up to the percent level for individual particles (Messenger et al., 2003; Busemann et al., 2009; Davidson et al., 2012). In the most pristine unequilibrated meteorites, matrix-normalized abundances of ∼200 ppm are observed (e.g., Nguyen et al., 2007, 2010; Floss and Stadermann, 2009; Vollmer et al., 2009; Nittler et al., 2013).

Oxide stardust grains are less abundant, with abundances of up to tens of ppm in meteorites (e.g., Vollmer et al., 2009; Leitner et al., 2012) and, on average, on the order of 20 ppm for IDPs, although concentrations for individual IDPs tend to be much higher, but contain large uncertainties, since they are based, in each case, on only one grain (Stadermann et al., 2006; Floss and Stadermann, 2009; Nguyen et al., 2014). The latter number is based on the identification of one single presolar Al_2O_3 grain and thus bears large uncertainties.

For material from comet 81P/Wild 2, statistics are limited. A distinction between presolar silicates and oxides is not possible for these samples, since all O-rich presolar signatures were found in high-velocity impact craters in aluminum foil, and structural information was largely erased in the impact process. To date, only 5 presolar O-rich grains have been found (Stadermann et al., 2008; Leitner et al., 2010; Floss et al., 2013).

Based on their O-isotopic compositions, presolar silicate and oxide grains are divided into four distinct groups, with a few "unusual" grains outside of this classification (Nittler et al., 1997, 2008).

Group 1 grains, which make up the majority of the presolar O-anomalous grains, have higher than solar $^{17}O/^{16}O$ and $^{18}O/^{16}O$ ratios ranging from ∼solar (2.01×10^{-3}) down to ∼1×10^{-3}. They formed in the outflows of 1.2–2.2 $M_\odot$ red giant and asymptotic giant branch (AGB) stars of approximately solar metallicity (the metallicity, Z, denotes the mass fraction of elements heavier than helium) (Nittler, 2009; Palmerini et al., 2011). Their O-isotopic compositions are well-explained by the so-called "first dredge-up" (FDU) process, which occurs when a star becomes a red giant star (e.g., Lattanzio and Boothroyd, 1997; Boothroyd and Sackmann, 1999). The products of partial H-burning are mixed into the convective envelope and modify the isotopic composition of the stellar surface. The $^{17}O/^{16}O$ ratio at the stellar surface is heavily influenced by this event and depends strongly on the stellar mass (e.g., El Eid, 1994; Boothroyd and Sackmann, 1999). The depth to which the convective envelope extends depends on the maximum temperature, and thus on the stellar mass. As can be seen from El Eid (1994) and Boothroyd and Sackmann (1999), this leads to a gradually enhancement of $^{17}O/^{16}O$ on the stellar surface until $M = 2$ to 2.5 $M_\odot$. For stars of higher masses, $^{17}O/^{16}O$ decreases again, because the convective envelope extends into region below the "^{17}O-peak" (El Eid, 1994), where ^{17}O is depleted. The $^{18}O/^{16}O$ ratio, on the other hand, is only slightly affected by the FDU, and mainly represents the initial composition of the stellar envelope.

Group 2 grains are also characterized by enhanced $^{17}O/^{16}O$ ratios, but are significantly depleted in ^{18}O ($^{18}O/^{16}O < 1 \times 10^{-3}$). These depletions cannot be explained by the first dredge-up in the parent stars, but require additional mixing processes, such as cool bottom processing (CBP) occurring in red giant and AGB stars with $M < 1.5\ M_\odot$ and sub-solar metallicity (Nollett et al., 2003; Palmerini et al., 2011), or hot bottom burning (HBB) in intermediate mass stars of 4–8 $M_\odot$ (Lugaro et al., 2017).

The origin of the grains of Group 3 is still not well-established. The majority of these grains show depletions in both ^{17}O and ^{18}O, pointing to a formation around red giant and AGB stars with low masses (<1.4 $M_\odot$) and low metallicities ($Z \leq Z_\odot$) (Nittler et al., 1997). According to Galactic chemical evolution (GCE) models, an increase of the $^{17,18}O/^{16}O$ ratios is expected with increasing metallicity. Thus, for low-metallicity stars one expects sub-solar $^{17,18}O/^{16}O$ ratios at the time of their birth (Timmes et al., 1995; Kobayashi et al., 2011). For stars with $M < 1.2\ M_\odot$, the first dredge-up should only have minor effects on the O-isotopic compositions (even at low metallicities) (Boothroyd and Sackmann, 1999). Combined, these effects can account for the majority of the Group 3 grains' isotopic compositions (Nittler, 2009). However, several Group 3 grains with sub-solar $^{17}O/^{18}O$ ratios are possibly of supernova origin (Nittler et al., 2008). Grains of Group 4 are characterized by significantly enhanced $^{18}O/^{16}O$ ratios, while the $^{17}O/^{16}O$ shows some variation. SNeII have been identified as their most probable stellar sources, based on a comparison of multi-element isotope data with model predictions (Nittler et al., 2008; Vollmer et al., 2008; Nguyen and Messenger, 2014).

Formation of O-rich and C-rich dust around AGB stars occurs during different evolutionary stages. Dust around low- and intermediate-mass AGB stars condenses almost exclusively during the thermal pulsing (TP-) AGB phase, while dust production on the First Giant Branch and in the early AGB-phase is very inefficient (Gail et al., 2009). Initially, the stellar envelope is O-rich (i.e., C/O < 1), which favors the formation of silicate and oxide stardust in the stellar outflow. After a series of thermal pulses, the star experiences a so-called "third dredge-up" (TDU), which mixes material from the He-intershell, including ^{12}C, to the stellar surface, resulting in a change of the envelope's composition. The carbon-to-oxygen ratio increases to C/O > 1, and the star becomes a carbon star, producing carbon and SiC dust (e.g., Gail et al., 2009, and references
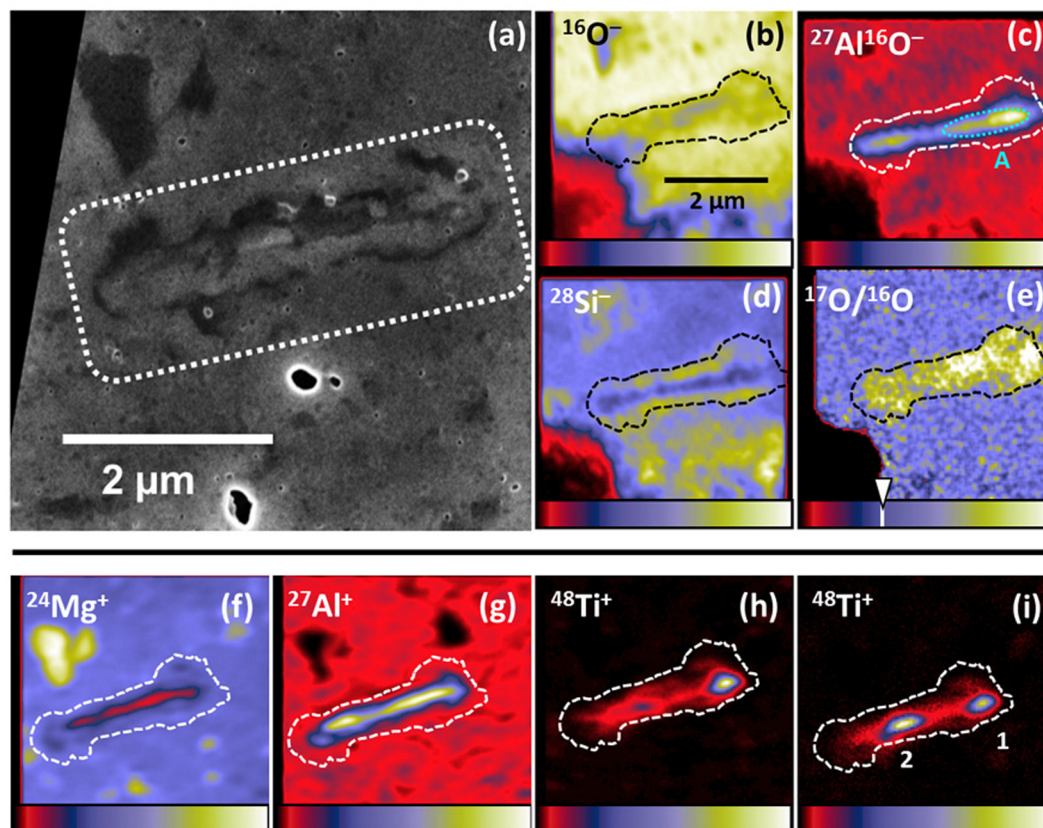
Fig. 1. (a) Electron micrograph of presolar grain KRY#I_37. The grain is located within the dotted white line, its outline darker than the surrounding matrix. (b) Secondary ion (SI) image of $^{16}O^-$. The area of the O-anomalous region is marked by the dotted line in this and the subsequent SI and isotope ratio images. (c) SI image of $^{27}Al^{16}O^-$. "A" refers to the part of the grain that was used to determine the Mg-isotopic composition and calculate the $^{26}Al/^{27}Al$ ratio (outlined by the light blue ellipse). (d) SI image of $^{28}Si^-$, revealing a Si-containing mantle around the central (Al-bearing) part of KRY#I_37. (e) $^{17}O/^{16}O$ ratio image. The presolar grain can be clearly distinguished from the surrounding matrix by its anomalous O-isotopic composition. The Solar System $^{17}O/^{16}O$ ratio is marked by the white line and triangle, and the maximum value displayed in the image is 8.4×10^{-4} (white color); apparent fluctuations of the $^{17}O/^{16}O$ ratio in the material surrounding the presolar grain are caused by counting statistics. (f) SI image of $^{24}Mg^+$. (g) Distribution of $^{27}Al^+$. (h) $^{48}Ti^+$ distribution at the beginning of the Mg-isotope measurement, and (i) $^{48}Ti^+$ distribution at the beginning of the Ti-isotope measurement (after the Mg-measurement). "1" and "2" denote the spots from which Ti-isotopic compositions were derived. The different position of the presolar grain in (b)–(e), (f)–(g) and (i) is due to the fact that the SI images were taken during different measurements. Field of view is 5×5 μm^2 for the SI and isotopic ratio images. The color bars represent a linear scale from black (zero intensity) to red and blue (low and intermediate intensity) to yellow and white (highest intensities). (For interpretation of the references to color in this figure legend, the reader is referred to the web version of this article.)

therein). However, model calculations for stars with initial masses $M \leq 1.5\,M_\odot$ and $Z \sim Z_\odot$ predict that the stellar envelope retains a C/O < 1 even after the onset of TDU episodes (Cristallo et al., 2011; F.R.U.I.T.Y. (Full-Network Repository of Updated Isotopic Tables & Yields) database[1]). Therefore, significant amounts of the He-burning products from the He-intershell could be incorporated in O-rich dust grains from these stars.

The first so-called "complex" presolar O-rich grain was reported by Vollmer et al. (2006) and consisted of an Al oxide core, surrounded by a silicate mantle. To date, less than a dozen of these "complex" or "compound" grains have been identified (Vollmer et al., 2006, 2009; Bose et al., 2012; Floss and Stadermann, 2012; Leitner et al., 2012; Nguyen et al., 2014; Takigawa et al., 2014).

Here, we report the isotopic and elemental compositions of a complex presolar grain (0.8 μm × 3.75 μm, Fig. 1(a)) from the Krymka ordinary chondrite (LL3.2), which is among the largest O-rich presolar grains found to date. The size of the grain allowed us to measure multiple isotope systems (O, Mg-Al, Si, and Ti), along with determining its elemental composition. A subsequent extraction of the grain by focused-ion beam lift-out for structural analyses by transmission electron microscopy (TEM) was, unfortunately, not successful. Preliminary results have been reported by Leitner et al. (2014, 2016) and Floss and Haenecour (2016).

2. EXPERIMENTAL

The presolar grain investigated here was found in a thin section of the Krymka LL3.2 ordinary chondrite from the collection of the Max Planck Institute for Chemistry

(MPIC) in Mainz, Germany. The thin section was initially characterized by scanning electron microscopy (SEM) at the MPIC, in the course of an investigation of the presolar grain inventories of fine-grained chondrule rims in so-called "cluster chondrite clasts" (CCCs) in ordinary chondrites (Leitner et al., 2014). These CCC-lithologies are characterized by close-fit textures of interlocking deformed and undeformed chondrules, and contain only low abundances of fine-grained material (Metzler, 2012). Krymka was included in our sample selection due its low petrologic type (3.2), and the fact that presolar oxide grains were identified in previous studies of grain separates from this meteorite (e.g., Nittler et al., 2008), as well as three presolar silicate grains by in situ ion imaging (Tonotani et al., 2006). Grain KRY#I_37 was identified, together with several presolar silicates, during a search for O-anomalous presolar grains by NanoSIMS in fine-grained chondrule rims surrounding chondrules in a CCC lithology of the Krymka thin section utilized in this study. No obvious veins or other indicators of secondary alteration were visible in the vicinity of the complex presolar grain (Fig. 1(a)).

The individual analysis steps were conducted in the following order:

(1) O-isotopic measurement (NanoSIMS) at "low" spatial resolution (100 nm Cs^+ beam)
(2) O-isotopic measurement (NanoSIMS) at "high" spatial resolution (60 nm Cs^+ beam)
(3) AES element mapping
(4) Si-isotopic measurement (NanoSIMS)
(5) Quantitative AES analyses
(6) Mg-Al-isotopic measurements (NanoSIMS)
(7) Ti-isotopic measurements (NanoSIMS)
(8) EDS analyses
(9) TOF-SIMS measurements

For the initial O-isotopic measurements, a Cs^+ primary beam (100 nm diameter, $\sim$1 pA) was rastered over 10×10 μm^2-sized sample areas (256×256 pixels) in semi-automated ("chained analysis") ion imaging mode. Prior to analysis, sample areas of 14×14 μm^2 were presputtered with a high current primary beam ($\sim$20 pA) to remove the carbon coating on selected regions.

A grain is considered presolar if its O-isotopic composition differs by at least 5.3σ from that of the surrounding matrix material (Hoppe et al., 2015). The measured O-isotopic composition of the presolar grain studied here was normalized to O-rich material in the surrounding matrix, which was assumed to have Solar System isotopic ratios. Isotopic compositions are either reported as ratios, or as "δ-values", displaying the deviation from a given standard value in per mil:

$$\delta(^A E/^B E) = \{[(^A E/^B E)_{meas}/(^A E/^B E)_{ref}] - 1\} \times 1000$$

with $^A E/^B E$ being the ratio of two isotopes of the element E with mass numbers A and B. "meas" denotes the measured value, and "ref" denotes the reference value. In this study, we use the abbreviated forms $\delta^{17,18}O$ for $\delta(^{17,18}O/^{16}O)$, $\delta^{25,26}Mg$ for $\delta(^{25,26}Mg/^{24}Mg)$, $\delta^{29,30}Si$ for $\delta(^{29,30}Si/^{28}Si)$, and $\delta^{47,49}Ti$ for $\delta(^{47,49}T/^{48}Ti)$.

2.1. High spatial-resolution O-isotope measurements

After this initial O-isotopic study, the grain was then re-measured at high spatial resolution with the NanoSIMS 50 at the MPIC. A Cs^+ primary beam with $\sim$60 nm diameter (0.1–0.2 pA) was rastered over a 5×5 μm^2 field of view centered on the presolar grain. Secondary ion (SI) images of $^{16,17,18}O^-$, $^{28}Si^-$, and $^{27}Al^{16}O^-$ were acquired in multi-collection mode. The complex nature of the grain is discernible from the SI images of $^{16}O^-$ (Fig. 1(b)), $^{27}Al^{16}O^-$ (Fig. 1(c)), and $^{28}Si^-$ (Fig. 1(d)), and the outline of the presolar grain denoted by the dashed line the was deduced from the $^{17}O/^{16}O$ ratio image (Fig. 1(e)). The total integration time was 130 min, divided into 5 image planes. The count rates of $^{16}O^-$ were corrected for quasi-simultaneous-arrivals (QSA) for each pixel in the ion images, using the theoretical QSA constant of 0.5 (Slodzian et al., 2004).

2.2. Si-isotopes

The Si isotopic composition of the grain was also measured with the NanoSIMS 50 at the MPIC, with a 100 nm Cs^+ beam (1 pA). Eight image planes (4 min each) were acquired over a 6×6 μm^2 sized area centered on the grain. SI images of $^{16,17}O^-$ and $^{28,29,30}Si^-$ were acquired in multi-collection mode, and the $^{28}Si^-$ count rate was QSA-corrected for each pixel in the ion images, applying the QSA constant of 0.6 from Hillion et al. (2008). The measured isotopic ratios were normalized to the average values of the surrounding matrix material, which were assumed to have Solar System isotopic compositions.

2.3. Mg- and Ti-isotopes

The Mg and Ti isotopic measurements were performed with a NanoSIMS 50L equipped with a new oxygen RF ion source at Cameca in Paris. Analyses were carried out with an O^- primary ion beam ($\sim$3 pA) at a lateral resolution of $\sim$100 nm. Six electron multipliers were used with two different mass sequences, by positioning the trolleys of the multi-collection unit at different masses, while the magnetic field remained constant. First, secondary ion images of $^{24,26}Mg^+$, $^{27}Al^+$, and $^{47,48,49}Ti^+$ were recorded in multi-collection mode. Second, the mass setting was changed to detect $^{24,25,26}Mg^+$ and $^{27}Al^+$ simultaneously. A Burma spinel standard was used for calibration of the Mg-isotopes as well as for the measured $^{27}Al^+/^{24}Mg^+$ ratios, and a perovskite standard was used to calibrate the Ti-isotopic data. From the $^{24}Mg^+$-distribution shown in Fig. 1(f), it is clearly visible that ^{24}Mg is predominantly located in the mantle area of the grain, while the core region is dominated by $^{27}Al^+$ (Fig. 1(g)). ^{48}Ti is distributed heterogeneously in the core, not only laterally, but also in depth, as can be seen from the $^{48}Ti^+$-images recorded at the beginning of the Mg-isotope measurement (Fig. 1(h)) and at the beginning of the subsequent Ti-isotope measurement (Fig. 1(i)). We selected a region with high Al/Mg (region "A" in Fig. 1(c)) to minimize the contribution of indigenous ^{26}Mg to the calculation of the $^{26}Al/^{27}Al$ ratio. For the

Ti-rich spots (depicted in Fig. 1(i)), the contribution of $^{48}Ca^+$ to the $^{48}Ti^+$ signal can be neglected, due to the relatively high Ti/Ca ratio of 10 determined by Auger electron spectroscopy (see below).

2.4. Auger Electron Spectroscopy (AES)

The major element composition of grain KRY#I_37 was analyzed with the PHI 700 Auger Nanoprobe at Washington University in St. Louis, using established procedures for presolar silicate grains (Stadermann et al., 2009). Auger electron energy spectra are obtained with a 10 kV primary electron beam (0.25 nA), which is rastered over the grain of interest; the spatial resolution achieved in this study was 10–20 nm. Typically, multiple spectral scans of a grain or point of interest are added together to obtain a single Auger spectrum, which is subjected to a 7-point Savitsky-Golay smoothing and differentiation routine prior to peak identification and quantification.

Relative sensitivity factors (RSFs) for the major rock-forming elements (O, Si, Fe, Mg, Ca, and Al) were determined from olivine and pyroxene standards of various compositions (Stadermann et al., 2009). For the quantification of Ti, no suitable standard was available, thus, the sensitivity factor from the built-in database was used. However, these sensitivity factors are matrix-dependent, and the direct application of the built-in RSFs might lead to large systematic errors (Stadermann et al., 2009). We compared the Ti concentrations obtained by AES with an estimate made from the Ti data measured by NanoSIMS (where a perovskite ($CaTiO_3$) standard was used), and found very good agreement of the results within error limits. Therefore, the Ti abundances measured by AES can be considered as reliable in this case. Reported errors are based on the 1σ uncertainties of the sensitivity factors (O: 3.6%; Si: 11%; Fe: 11.2%; Mg: 9.4%; Ca: 10.8%; Al: 24.9%, Ti: 10%) and should be considered lower limits, since they do not include a correction for background noise, or take into account other factors that can affect the quality of a spectrum (e.g., sample charging, residual surface contamination). Detection limits are element-dependent, but typically in the range of a few atom percent. In addition, elemental distribution maps of grain KRY#I_37 and the surrounding meteorite matrix were acquired.

2.5. Energy-dispersive X-ray Spectroscopy

The presolar grain studied here was imaged by scanning electron microscopy with a LEO 1530 Field Emission Scanning Electron Microscope (FE-SEM) after its detection by O-isotope mapping (Fig. 1). Quantitative elemental data, as well as element distribution maps, were acquired by energy-dispersive X-ray spectroscopy (EDS), utilizing an Oxford X-max 80 silicon drift EDS detector attached to the LEO 1530 FE-SEM at the Max Planck Institute for Chemistry (MPIC) in Mainz. For data acquisition, Oxford's INCA and Aztec software suites were utilized. Quantitative element data were obtained without external standards. The accuracy of the system was determined by measuring a suite of standard minerals with known compositions: diopside

(BM.2005,M310 from Yates Mine, Quebec, Canada), olivine (BM.1950,337 from the Admire pallasite meteorite), bytownite (BM.2005,M312, from Majorqap qava in Greenland), and pyrrhotite (BM.2005,M317 from Drag in Norway). Compositions of the individual mineral standards were reproduced with >99% accuracy.

2.6. Time-of-flight secondary ion mass spectrometry (TOF-SIMS)

The elemental composition of KRY#I_37 was also analyzed using the IDLE3 TOF-SIMS instrument at the School of Earth and Environmental Sciences at the University of Manchester. The basic layout of the IDLE instruments is described in Henkel et al. (2006, 2007a). The measurements for this study were performed with a 25 kV Au_n^+ liquid metal ion gun (LMIG), using an Au^+ primary ion beam with ~500 nm spatial resolution. For the detection of intermediate-mass (trace) elements, the delayed-extraction mode was applied, and the sample was sputter-cleaned prior to analysis to remove surface contamination. In the delayed extraction mode, a mass resolving power of m/Δm ~ 3000 was achieved (see also King et al., 2010), which allowed to resolve relevant molecular mass interferences. Raw data were collected for offline analysis. Element abundances (in at.%) relative to the Si-abundance were calculated with the RSFs determined by King et al. (2010) for Au^+ primary ions and delayed extraction mode.

The region of interest for KRY#I_37 was defined using the $^{27}Al^+$, $^{28}Si^+$, $^{40}Ca^+$, and $^{48}Ti^+$ secondary ion distributions to mark the grain area and obtain a bulk spectrum for the grain. Lateral shifts of the grain position within the field of view were corrected during data analysis after acquisition.

3. RESULTS

3.1. Isotopic compositions

The grain has an O-isotopic composition of $^{17}O/^{16}O = (8.40 \pm 0.16) \times 10^{-4}$ and $^{18}O/^{16}O = (1.83 \pm 0.03) \times 10^{-3}$, placing it well within the isotopic compositions of Group 1 silicates and oxides, as can be seen in Fig. 2 and Table 1 (Nittler et al., 1997, 2008).

We determined the Mg-isotopic composition from the innermost part of the core, with a high $^{27}Al^+/^{24}Mg^+$ ratio of 9.4 (region "A" in Fig. 1(c)). After correcting for instrumental mass fractionation (IMF), we find a small positive ^{26}Mg-anomaly of $\Delta^{26}Mg = (45 \pm 12)‰$ (with $\Delta^{26}Mg = \delta^{26}Mg - 2 \times \delta^{25}Mg$), likely due to the presence of radiogenic ^{26}Mg from the decay of ^{26}Al. We then calculate an initial $^{26}Al/^{27}Al$ ratio of $(^{26}Al/^{27}Al)_{ini} = (4 \pm 1) \times 10^{-4}$, as displayed in Fig. 3 and Table 2, using the equation given in Nittler et al. (2008):

$$(^{26}Al/^{27}Al) = [(^{26}Mg*/^{24}Mg)_{meas} - (^{26}Mg/^{24}Mg)_{ref}]/[(^{27}Al/^{24}Mg)_{meas} \times \Gamma]$$

with $(^{26}Mg*/^{24}Mg)_{meas}$ inferred from the IMF-corrected $\Delta^{26}Mg$, $(^{26}Mg/^{24}Mg)_{ref} = 0.13932$ (Catanzaro et al., 1966), and the (experimentally derived) sensitivity factor Γ with
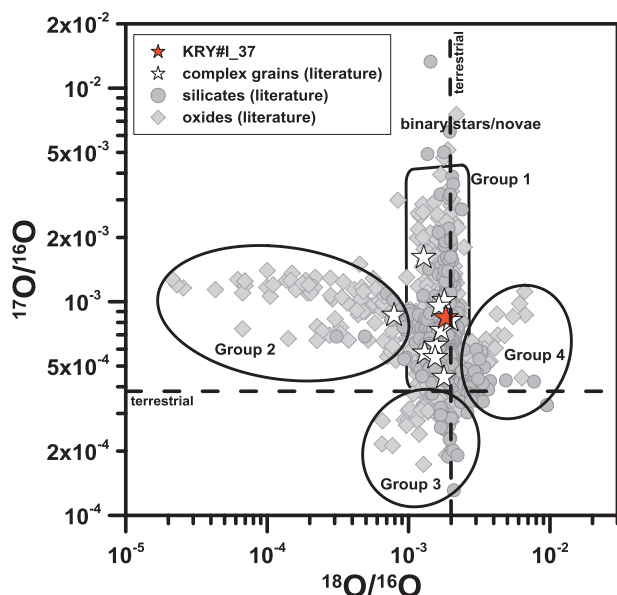
Fig. 2. Oxygen isotopic composition of KRY#I_37 compared with complex grains from other studies (listed in Table 1). Grain groups (Nittler et al., 1997, 2008) are symbolized by black continuous lines. For comparison, data for presolar silicate (grey circles) and oxide (grey diamonds) grains from the literature are plotted (Bland et al., 2007; Bose et al., 2010; Bose et al., 2012; Choi et al., 1998; Floss and Stadermann, 2009; Floss and Stadermann, 2012; Leitner et al., 2012; Mostefaoui and Hoppe, 2004; Nguyen and Zinner, 2004; Nguyen et al., 2007, 2010; Nittler et al., 1997; Nittler et al., 2008; Vollmer et al., 2009; Zhao et al., 2013; Zinner et al., 2003). Errors are 1σ; terrestrial ratios are indicated by the dashed lines.

$\Gamma = 1.56$ (taken from measurements on spinel; Hoppe et al., 2010).

Ti isotopes were measured in two Ti-rich spots ("1" and "2" Fig. 1 (i)). No significant deviations from the Solar System value were observed ($\delta^{47}Ti = -8 \pm 10‰$ and $\delta^{49}Ti = 23 \pm 11‰$ for spot 1, and $\delta^{47}Ti = 11 \pm 9‰$ and $\delta^{49}Ti = 3 \pm 9‰$ for spot 2) (Fig. 4, Table 2). The Si isotopic composition shows no large deviation from the Solar System value for $^{29}Si/^{28}Si$, with $\delta^{29}Si = 11 \pm 4‰$. For $^{30}Si/^{28}Si$, on the other hand, we observe a small but significant excess in ^{30}Si, with $\delta^{30}Si = 41 \pm 5‰$ (Fig. 5, Table 2).

3.2. Auger electron spectroscopy and energy-dispersive X-ray spectroscopy results: elemental compositions

Element mapping by Auger electron spectroscopy revealed that the core region of the complex grain consists not only of Al-oxide, but also contains Ca and Ti. This is displayed in Fig. 6, and the elemental concentrations are given in Table 3. The distributions of Al, Ca, and Ti do not fully correlate. We note a Ti-rich region on the very right edge of the core, while Al shows the highest concentrations in two sub-areas (labeled "A" and "B" in Fig. 6) in the left and right part of the central region (however, the sub-area on the right side is not correlated with the Ti-hotspot). Ca is also heterogeneously distributed and is present in the core, as well as the mantle region of the grain.

The presence of Si is restricted to the mantle, and also shows some heterogeneity. Quantitative results show that the core of KRY#I_37 mainly consists of Al- and Ti-oxide (O = 56 at.%, Al = 30 at.%, Ti = 11 at.%), together with contributions of Ca (1.5 at.%) and Fe (2.6 at.%) (Table 3). As can be seen from Fig. 6, patches of Fe within the grain area are almost exclusively located in the mantle region, and are generally anti-correlated with the regions that show high intensities of Ca and Si. The mantle shows high abundances of O and Si (65 at.% and 30 at.%, respectively), with minor amounts of Mg (1.1 at.%), Ca (1.3 at.%), and Fe (2.8 at.%). For the Ti-rich area (Fig. 6, and "Ti-spot 1" in Fig. 1), we observe a high abundance of Fe (20 at.%), Ti (14 at.%), Al (13 at.%) and O (51 at.%); for Ti-spot 2, we could not acquire quantitative data, since it became visible during the Mg-Al-isotope measurements, after the AES analyses were conducted.

X-ray elemental maps were obtained with acceleration voltages from 3.5 kV to 10 kV (Fig. 7). From these maps, the Al-rich core of the grain can be easily identified; and Mg and Si are visible in the mantle of KRY#I_37. Ca is also clearly present in the grain and a pronounced Ti-hotspot is observed (corresponding to "Ti-spot 2" from Fig. 1), as well as a less pronounced spot at the position of "Ti-spot 1", together with a P-bearing spot. Quantitative SEM-EDS measurements of the mantle area of the grain and the surrounding matrix were carried out with an acceleration voltage of 8 kV. This voltage was required to ensure reliable signal intensities for all elements detected in the grain. With the lateral resolution of 500–600 nm achieved under these conditions, the obtained element abundances clearly contain contributions from the surrounding matrix. However, by comparing the data with the composition of the surrounding matrix (Figs. 6 and 7, Table 3), it is possible to determine which elements might be affected by dilution from the surrounding material. Al, Ca, and Ti are only present at low levels or below detection limits in the surrounding matrix and, therefore, their abundances can be considered to be undiluted within the presolar grain. The matrix contains ~5 at.% Mg, while the abundance is slightly higher in the grain mantle (~8 at.%). For Fe, concentrations in the vicinity of KRY#I_37 are comparably high (~20 at.%), while we observe ~5 at.% in the grain's mantle. The concentrations for Mg and Fe given here are not corrected for dilution effects from the surrounding matrix. If we consider a contribution of ~30% from the matrix to the measured Mg-abundance in the mantle, we estimate the "true Mg-abundance to be ≤10 at.%. From the NanoSIMS-derived Mg-data, we estimated a concentration of ~8–9 at.% in the mantle. Thus, the rough estimate of ~30% for the dilution factor seems to be reasonable. By applying this factor to the Fe-abundance, we estimate that the "true" Fe-concentration in the mantle is <0.3 at.%.

The discrepancy that we observe between the mantle compositions determined by AES and EDS (Table 3) can be explained by the different volumes that are sampled by the two techniques. While the AES data were determined with a spatial resolution of ~20 nm and a sampling depth of a few nm, the respective parameters for the quantitative EDS measurements (performed with 8 kV acceleration

Table 1
Isotopic compositions of grain KRY#I_37 and complex grains reported in the literature. All errors are 1σ.

Grain	Ref.[a]	$^{17}O/^{16}O$ ($\times 10^{-4}$)	$^{18}O/^{16}O$ ($\times 10^{-3}$)	Group	$M_{star}/M_\odot$[b]	$(^{18}O/^{16}O)_{ini}/(^{18}O/^{16}O)_\odot$[b]	Size (nm)
KRY#I_37	This work	8.40 ± 0.16	1.83 ± 0.02	1	1.5	1.15	3750 × 800
7_04b	V06	5.74 ± 0.15	1.30 ± 0.02	1	1.4	0.85	1000 × 600
32_03b	V09	10.10 ± 0.49	1.79 ± 0.06	1	1.6	1.05	600 × 500
22_09b[d]	V09	8.63 ± 0.63	0.79 ± 0.06	2	n.d	n.d.	670 × 480
51-1[e]	B12	8.16 ± 0.26	1.98 ± 0.04	1	1.5	1.2	380 × 340
51-8[f]	B12	9.51 ± 0.19	1.64 ± 0.03	1	1.6	0.95	570 × 570
3a-1-o2c	FS12	4.42 ± 0.10	1.78 ± 0.02	1	1.2	1.05	480 × 480
5a-1-o2	FS12	5.47 ± 0.19	1.54 ± 0.03	1	1.4	0.9	315 × 315
"W2027E6 slice#6"[c,g]	N14	7.33 ± 0.27	1.70 ± 0.04	1	1.4–1.5	1.0	345 × 260
6_8[h]	L12	6.24 ± 0.12	1.56 ± 0.02	1	1.4	0.9	1,750 × 300
Bish60-35[i]	T14	16.10 ± 0.10	1.28 ± 0.01	1	1.8	0.85	1,000 × 800
Solar system		3.81	2.01				

[a] References. V06: Vollmer et al., 2006; V09: Vollmer et al., 2009; B12: Bose et al., 2012; FS12: Floss and Stadermann, 2012; N14: Nguyen et al., 2014; L12: Leitner et al., 2012; T14: Takigawa et al., 2014.
[b] Interpolated by comparison with grain data from Nittler et al. (2008).
[c] No grain label reported.
[d] complex grain with multiple phases and a core.
[e] Two subgrains; one olivine, one Fe-rich non-stoichiometric silicate.
[f] Multiple subgrains, Ca-pyroxene and Fe-rich non-stoichiometric silicate.
[g] Spinel core with Ti, Fe; Mg- and Si-rich silicate rim.
[h] Hibonite with Ti-oxide subgrain.
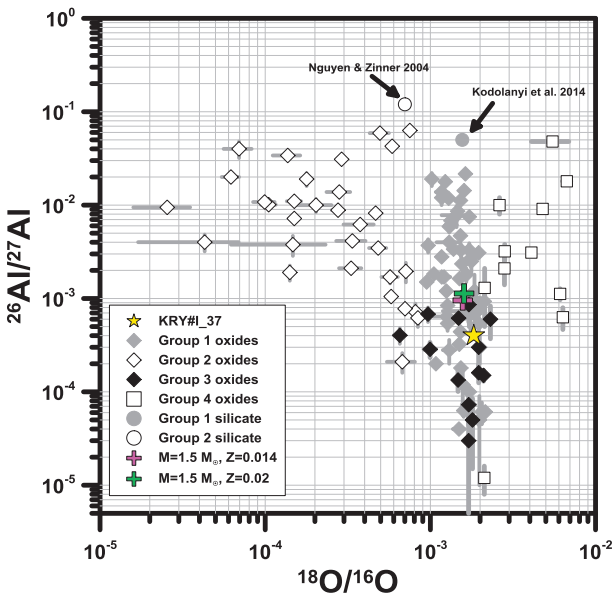[i] Al_2O_3 with Ti-oxide subgrain.

Fig. 3. $^{18}O/^{16}O$ ratios versus inferred $^{26}Al/^{27}Al$ ratios for the complex grain KRY#I_37 together with literature data for presolar oxide grains (Huss et al., 1994; Hutcheon et al., 1994; Nittler et al., 1994; Nittler et al., 1997; Choi et al., 1998; Choi et al., 1999; Krestina et al., 2002; Nittler et al., 2005; Zinner et al., 2005; Nittler et al., 2008), and 2 presolar silicate grains (Nguyen and Zinner, 2004; Kodólanyí et al., 2014). The cross symbols in magenta and green denote the calculated data for AGB stars from the F.R.U.I.T.Y. models considered here. All errors are 1σ.

voltage) were 500–600 nm spatial resolution and ~400 nm sampling depth. Thus, if the elements were distributed heterogeneously in the mantle, this would be reflected in the abundances obtained by AES and EDS.

Table 2
Mg-, Si-, and Ti-isotopic compositions of grain KRY#I_37. All errors are 1σ.

		Remarks
$\delta^{25}Mg$ (‰)	−19 ± 7	Region A[b]
$\delta^{26}Mg$ (‰)	7 ± 7	Region A
$\Delta^{26}Mg$ (‰)[a]	45 ± 12	Region A
$^{27}Al/^{24}Mg$	9.4	Region A
$(^{26}Al/^{27}Al)_{ini}$[a]	(4 ± 1)×10^{-4}	Region A
$\delta^{29}Si$ (‰)	11 ± 4	Mantle
$\delta^{30}Si$ (‰)	41 ± 5	Mantle
$\delta^{47}Ti$ (‰)	−8 ± 10	Ti-Spot 1[b]
$\delta^{47}Ti$ (‰)	11 ± 9	Ti-Spot 2[b]
$\delta^{49}Ti$ (‰)	23 ± 11	Ti-Spot 1
$\delta^{49}Ti$ (‰)	3 ± 9	Ti-Spot 2

[a] See Section 3.1 for the calculation of these quantities.
[b] See Fig. 1 for the respective areas.

3.3. TOF-SIMS results: Intermediate-mass elements/trace elements

Due to the TOF-SIMS spatial resolution of ~500 nm, no exact distinction between the core and mantle region of the grain was possible. However, as can be seen from the secondary ion images displayed in Fig. 8, the grain's core can be identified from the $^{27}Al^+$, $^{40}Ca^+$, $^{27}Al^{16}O^-$, and $^{48}Ti^+$ maps, while $^{24}Mg^+$ and $^{28}Si^+$ appear to be enhanced in the outer region of the grain. Mg and Fe show slightly lower abundances in the grain area than in the surrounding matrix (factors of ~0.9 and ~0.8, respectively); for Mg, the matrix abundance is dominated by a large forsterite grain located in the upper left part of the field of view. Al, Ca, and Ti show clear enrichments in the grain
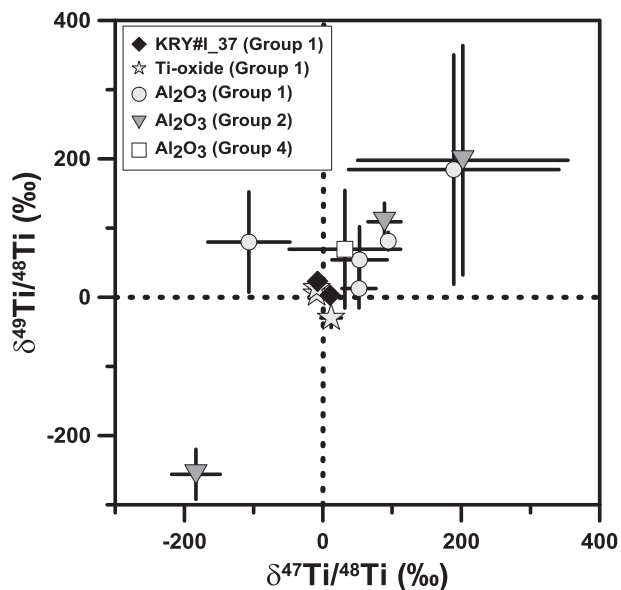
Fig. 4. Ti-isotopic compositions of the two Ti-rich spots measured in KRY#I_37, together with reference data for O-rich presolar oxide grains from Choi et al., 1998; Huss et al., 1994; Hutcheon et al., 1994; Nittler et al., 2005, 2008; Strebel et al., 1997. Compositions are displayed as deviations from the Solar System ratios (denoted by the dotted lines) in per mil. All errors are 1σ; if no errors bars are visible, the respective errors are smaller than the displayed symbols.
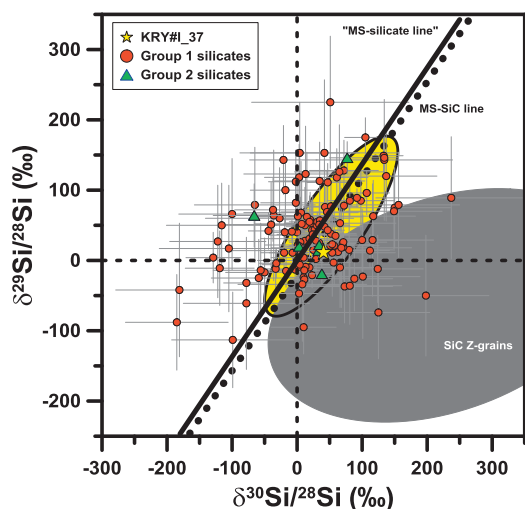

Fig. 5. Three-isotope plot for silicon. Compositions are displayed as δ-values; the Solar System composition is denoted by the dashed lines. For comparison, the Si-isotopic compositions for Group 1 and 2 silicates are shown (Busemann et al., 2009; Leitner et al., 2012; Mostefaoui and Hoppe, 2004; Nagashima et al., 2004; Nguyen et al., 2007, 2010; Vollmer et al., 2008). The range of Si-isotopic compositions for mainstream SiC and SiC of type Z are marked by the yellow and gray ellipse, respectively, the dotted line denotes the SiC mainstream line (Zinner et al., 2006), and the black continuous line denotes the "silicate mainstream line" from Vollmer et al. (2008). All errors are 1σ. (For interpretation of the references to color in this figure legend, the reader is referred to the web version of this article.)

area, with enrichment factors ranging from 2 to 5. In the mass range of 50–100 u, only a few ion species were identified above detection limit that can be clearly associated with the grain area. These are shown in Fig. 8 and Table 4; since the spatial resolution of the TOF-SIMS measurements cannot fully exclude dilution effects from surrounding matrix, the TOF-SIMS-derived ratios discussed here should be considered lower limits. Apart from the elements already identified by EDS and AES, the TOF-SIMS investigation showed the presence of V (Fig. 8, Table 4), with an abundance 2.7 times higher than in the surrounding matrix. Rb shows a slightly higher concentration in the grain; however, this is only significant on a 2σ-level, while Sr is enriched by a factor of 1.5 ± 0.1 (Table 4).

Abundance estimates from the SI intensities are somewhat complicated in this special case. For quantification with TOF-SIMS, relative sensitivity factors are required. These are well-known and established (Stephan, 2001; King et al., 2010), but introduce additional uncertainties to the calculations. Abundances derived by this method are typically expressed as *relative* abundances, with Si as the reference element. This could theoretically pose a problem for the current study, since the distributions of the major elements are not well correlated with Si, and in the case of Al and Ti even show an anti-correlation (Fig. 6). However, for the spatial resolution achieved here ($\sim$500 nm), it is valid to consider the element distributions for the major elements (Mg, Al, Si, Ca) as homogeneous. We obtain Si-normalized abundances of 26×10^{-3} for Ti, 7×10^{-4} for V, 2.4×10^{-5} for Rb, and 2.0×10^{-4} for Sr.

We were also able to confirm the presence of P in a sub-region of the complex grain. While $^{31}P^-$ typically has a low ionization yield, the $^{31}P^{16}O^-$, $^{31}P^{16}O_2^-$ and $^{31}P^{16}O_3^-$ maps (Fig. 8) show higher SI intensities. Especially for $^{31}P^{16}O_2^-$ and $^{31}P^{16}O_3^-$, we observe a localized spot with higher intensity on the left end (Fig. 8) of the grain, at the same position where P was detected by EDS (Fig. 7). The high surface sensitivity of the TOF-SIMS measurement (depth information is obtained from the uppermost 5 atomic monolayers) revealed that the P detected by EDS (Fig. 7) is indeed located in the grain, and does not come from an underlying matrix grain. Moreover, the presence of the $^{31}P^{16}O_x^-$ ions shows that the phosphorus is located in a P-O-phase, possibly a phosphate.

4. DISCUSSION

4.1. Stellar origin

Nine of the ten complex presolar grains discovered prior to this study belong to Group 1, with $^{17}O/^{16}O$ ratios suggesting origins from AGB stars with masses ranging from $1.2\,M_\odot$ to $1.8\,M_\odot$, and initial $^{18}O/^{16}O$ ratios (as approximation for the stellar metallicity) of 0.85–1.2 times the solar value (Table 1; both quantities interpolated from the data set given in Nittler et al. (2008)). Comparison of the O-isotopic data of grain KRY#I_37 with the stellar properties inferred by Nittler et al. (2008) for presolar Group 1 oxide grains yields a stellar mass of $\sim$1.5 $M_\odot$ and an initial $^{18}O/^{16}O$ ratio $\sim$15% higher than solar. The initial
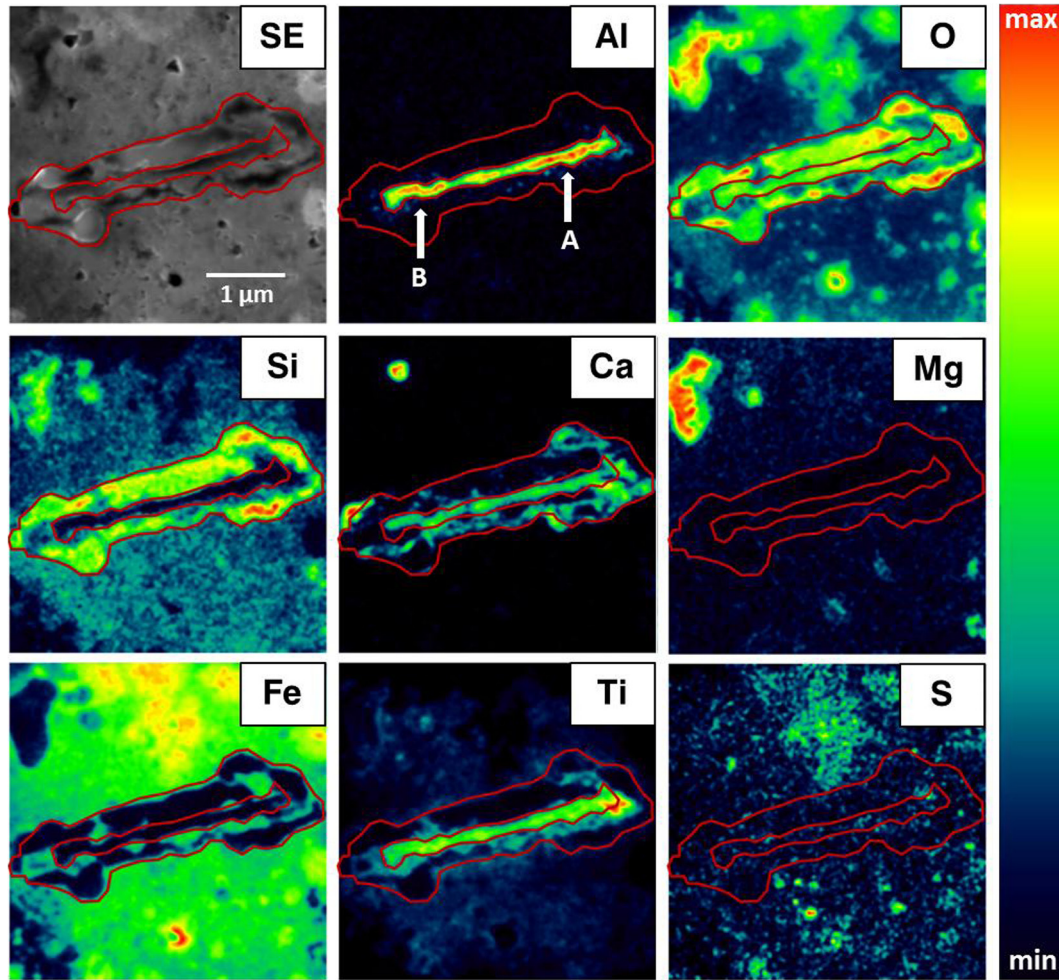
Fig. 6. Secondary electron (SE) image and false color element maps determined by AES. The presolar grain and its core region are outlined in red. For Al, the regions with the highest intensities are marked with the white arrows and labeled "A" and "B" (see text). The field of view for all panels is 4×4 µm^2. The color bar represents a linear scale from black (zero intensity) to red (maximum intensity). (For interpretation of the references to color in this figure legend, the reader is referred to the web version of this article.)

Table 3
Elemental composition of grain KRY#I_37 by AES and SEM-EDS (concentrations are given in atom percent). All errors are 1σ.

	O (at.%)	Mg (at.%)	Al (at.%)	Si (at.%)	Ca (at.%)	Ti (at.%)	Fe (at.%)
Core (AES) ($n = 2$)[a]	56 ± 2	b.d.[b]	30 ± 7	b.d	1.5 ± 0.2	11 ± 1	2.6 ± 0.6
Ti-rich spot 1 (AES)	51 ± 2	b.d.	13 ± 3	b.d.	1.4 ± 0.1	14 ± 1	20 ± 2
Mantle (AES) ($n = 4$)	65 ± 2	1.1 ± 0.3	b.d.	30 ± 3	1.3 ± 0.3	b.d.	2.8 ± 0.6
Mantle (EDS) ($n = 4$)	62 ± 2	8.3 ± 0.4	b.d.	15.8 ± 0.6	9.1 ± 0.6	b.d.	5 ± 1
Matrix (AES)	52 ± 2	4.9 ± 0.5	b.d.	12 ± 1	b.d.	b.d.	31 ± 4
Matrix (EDS) ($n = 5$)	58.4 ± 0.8	5.5 ± 0.1	1.2 ± 0.1	14.2 ± 0.2	0.2 ± 0.1	b.d.	20.6 ± 0.2

[a] n denotes the number of individual analyses from which the respective abundances were calculated.
[b] Below detection limit.

^{18}O/^{16}O-ratio is reduced during the first-dredge-up (FDU) by ~15–35%, depending on mass and metallicity of the star, when ^{18}O-poor material from the H-burning zone is mixed to the surface of the star. ^{18}O is destroyed in the CNO-cycle during H-burning, by the reaction ^{18}O(p,α)^{15}N, while ^{17}O is enhanced by the decay of ^{17}F (^{17}F → ^{17}O + e$^+$ + ν$_e$), which is synthesized by ^{16}O(p,γ)^{17}F.

By investigating the 1.5 M$_\odot$ stellar models with Z = 0.014 and Z = 0.02 from the F.R.U.I.T.Y. database[2] (Cristallo et al., 2011), we find ^{26}Al/^{27}Al ratios of (9.5–11.3) × 10^{-4} at the time of the first TDU event. The pres-
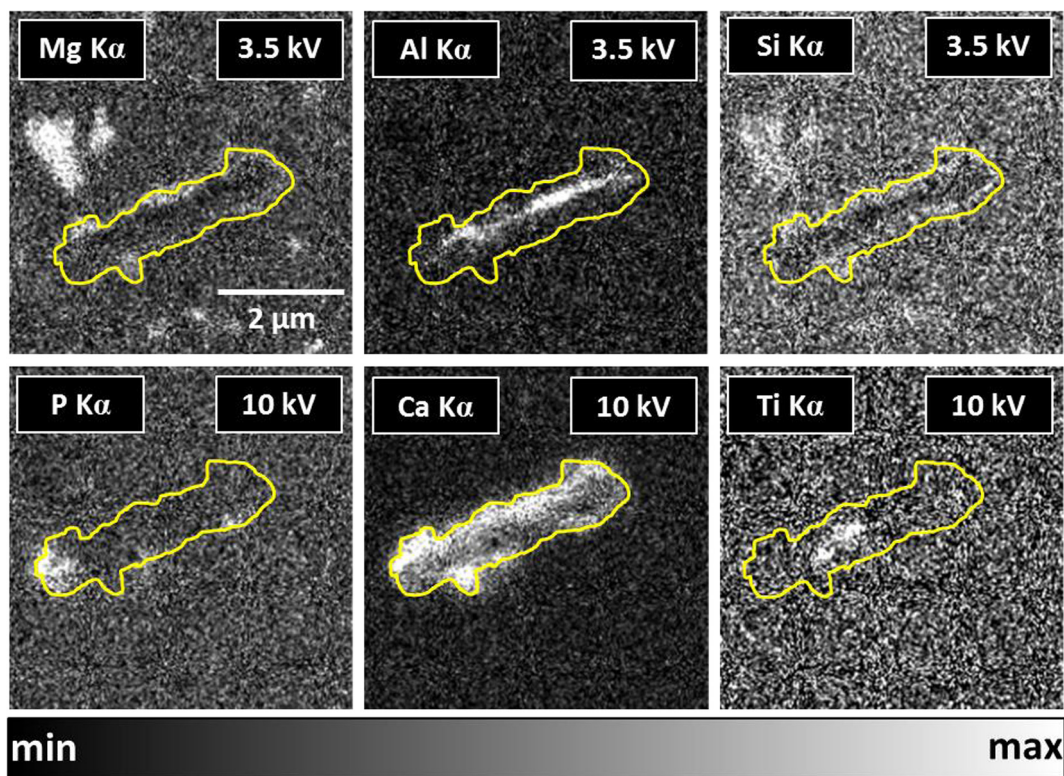
Fig. 7. Element distributions for Mg, Al, Si, P, Ca, and Ti determined by SEM-EDS. Scale bars are displayed on the left side below each panel. The acceleration voltages at which the data were acquired are shown in the lower left corners, and the respective lines used to generate the distribution maps are shown above the individual panels. The greyscale bar represents a linear scale from black (zero intensity) to white (maximum intensity).

ence of ^{26}Al can be used as an indicator for the timing of grain condensation. It is produced via the reaction ^{25}Mg $(p,\gamma)^{26}$Al in the H-burning shell of an AGB star, and is transported to the stellar surface during TDU episodes, and is incorporated into condensing circumstellar dust (e.g., Zinner et al., 2005 and references therein). Since the time between thermal cycles (i.e., TDU episodes) is shorter than the half-life of ^{26}Al of ~700,000 years (Zinner et al., 2005), the ^{26}Al/^{27}Al ratios in the stellar envelope evolve with time, and allow an estimate for the timing of grain formation. The absence of ^{26}Al would indicate condensation of the dust grain prior to the onset of TDU, while its presence implies formation at least during the first TDU event.

For the mass and metallicity ranges considered above, the stellar envelope retains a C/O-ratio < 1 even after several TDU episodes. Thus, condensation of O-rich dust would have been possible even after the composition of the star's surface has been modified by addition of He-burning products. The $(^{26}$Al/^{27}Al)$_{ini}$ ratio of $(4 \pm 1) \times 10^{-4}$ that we determined for grain KRY#I_37 is 2.5 times lower than in the model predictions, but lies well within the range of ^{26}Al/^{27}Al ratios observed for O-rich presolar grains of Group 1 (Fig. 3).

However, we note that there are several uncertainties that must be considered: (i) The relative Al/Mg sensitivity factor required to calculate ^{26}Al/^{27}Al was determined on spinel, which might be inappropriate for the material considered here, and a systematic uncertainty of >20% must be considered. (ii) For the calculation of the ^{26}Mg excess we assumed that ^{25}Mg/^{24}Mg is solar. However, if the true δ^{25}Mg were, e.g., +10‰, which is not unrealistic in view of Mg isotope data for Group 1 silicates (Kodólanyí et al., 2014), then the calculated ^{26}Al/^{27}Al would be about 1.5 times higher. (iii) Current models on ^{26}Al production in AGB stars bear large uncertainties (see discussion in Nittler et al., 2008). Taking all this into account, the observed discrepancy of a factor of 2.5 between the measured and predicted ^{26}Al/^{27}Al is reasonable.

An "early" formation after FDU and at the onset of the TDU episodes is also supported by the Ti-isotopic composition of the grain. Wasserburg et al. (2015) found that for a "late" formation of circumstellar dust, i.e., after the star entered the TDU phase, enhanced ^{47}Ti/^{48}Ti and ^{49}Ti/^{48}Ti ratios are to be expected, representing the nucleosynthetic fingerprint of the material modified by the s-process. This process (also called "slow-neutron-capture-process" in unabridged form) is a nucleosynthetic process operating in the He-rich intershell region of AGB stars. The s-process occurs at comparably low neutron densities, supplied by the reactions ^{13}C$(\alpha,n)^{16}$O and ^{22}Ne$(\alpha,n)^{25}$Mg (the latter reaction only plays a minor role for low-mass AGB stars, since it is only marginally activated at the temperature reached in these stars). Neutron capture takes place
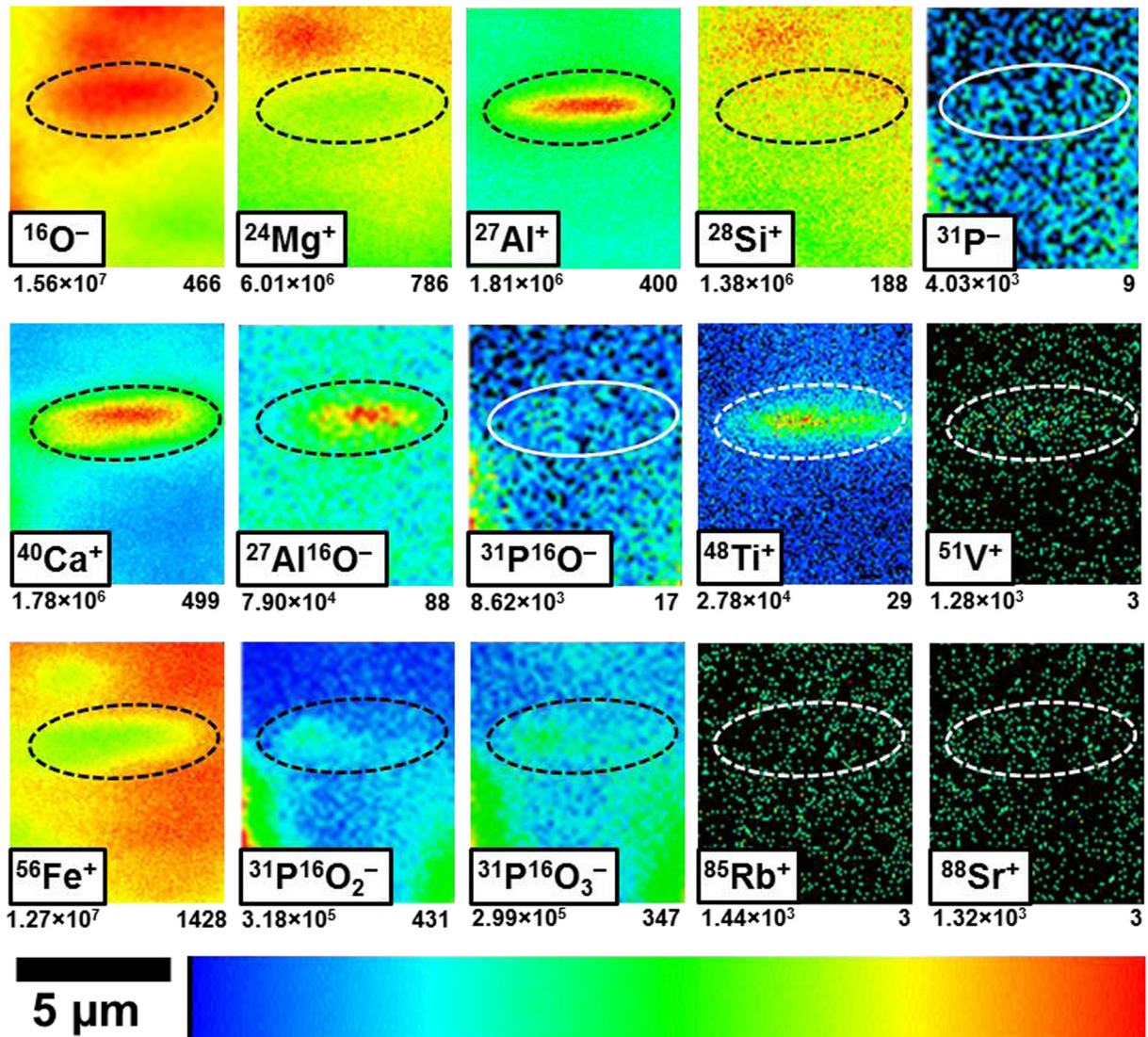
Fig. 8. Element distributions measured by TOF-SIMS. The ion species is denoted in the upper left corner of each image. Below each image, the maximum intensity per pixel to which the ion image is normalized, and the integrated intensity of the whole image are given. The color bar represents a linear scale from black (zero intensity) to red (maximum intensity). (For interpretation of the references to color in this figure legend, the reader is referred to the web version of this article.)

on comparably long time scales ($\sim 10^2$ to 10^5 a for each capture), resulting in a "slow" rate in comparison to the intervening β-decay reactions (e.g., Burbidge et al., 1957; Gallino et al., 1997). In this way, a large number of the isotopes in the range $23 \leq A \leq 46$ and $63 \leq A \leq 209$ are produced (Burbidge et al., 1957). The products of this process are then mixed to the stellar process by TDU events; i.e., observation of isotopic compositions characteristic for s-processing also supports formation of the respective presolar grain after the onset of TDU.

In the case of formation early in the AGB-phase, the Ti-isotopes are dominated by the initial composition of the stellar material, since no or only very little s-process Ti has been mixed to the surface in this stage of stellar evolution. For KRY#I_37, we observed no significant deviation from the solar value for the Ti-isotopic composition (Fig. 4).

The Si-isotopic composition of KRY#I_37 is compatible with the values of SiC Z-grains, which show signs of s-process Si mixed to the stellar surface by TDU, as well as with the range observed for mainstream (MS) and SiC-Y grains (Fig. 5). However, the stellar sources for SiC Y and Z grains show characteristics that are incompatible with the presumed parent star of the complex grain KRY#I_37: SiC Z-grains come from stars with significantly lower-than-solar metallicities ($Z \sim 1/3 \times Z_\odot$, Hoppe et al., 1997), and such an origin is not supported for KRY#I_37 by its O- and Ti-isotopic compositions. A Z-grain-like metallicity would be clearly visible from the $^{18}O/^{16}O$-ratio, which would be 20–25% lower than the one measured here (derived from the F.R.U.I.T.Y. database). Also, if the ^{30}Si-excess was due to a contribution of s-process Si from the stellar interior of a star with a metallicity of $Z \sim 1/3 \times Z_\odot$, the $^{47}Ti/^{48}Ti$ and $^{49}Ti/^{48}Ti$ ratios would be

Table 4
Secondary ion intensities normalized to Si obtained by TOF-SIMS for grain KRY#I_37 and the surrounding matrix. Also shown are the respective ratios of these intensities, as well as the Si-normalized abundances (in atom percent) determined for the grain area.

Element	KRY#I_37 Int.(E)/Int.(Si)	Matrix[a] Int.(E)/Int.(Si)	$(R^{Int}_{E,Si})_{grain}/(R^{Int}_{E,Si})_{matrix}$ [b]	KRY#I_37 Abd.(E)/Abd.(Si)[c]	err(+)[d]	err(−)[d]
Mg	4.8 ± 0.1	5.4 ± 0.1	0.88 ± 0.02	1.1	0.3	0.2
Al	2.19 ± 0.04	1.16 ± 0.02	1.89 ± 0.03	0.4	0.1	0.1
Ca	2.84 ± 0.04	0.93 ± 0.02	3.1 ± 0.1	0.3	0.1	0.1
Ti	0.101 ± 0.002	0.019 ± 0.001	5.3 ± 0.3	26×10^{-3}	5×10^{-3}	5×10^{-3}
V	$(23 \pm 2) \times 10^{-4}$	$(8.4 \pm 0.5) \times 10^{-4}$	2.7 ± 0.3	7×10^{-4}	2×10^{-4}	2×10^{-4}
Fe	7.1 ± 0.1	9.2 ± 0.2	0.77 ± 0.02	3.4	1.4	1.0
Rb	$(11 \pm 1) \times 10^{-4}$	$(8.9 \pm 0.7) \times 10^{-4}$	1.2 ± 0.1	24×10^{-6}	9×10^{-6}	7×10^{-6}
Sr	$(12 \pm 1) \times 10^{-4}$	$(8.1 \pm 0.3) \times 10^{-4}$	1.5 ± 0.1	2.0×10^{-4}	1.2×10^{-4}	0.8×10^{-4}

[a] Normalized intensities from the surrounding meteorite matrix.
[b] $(R^{Int}_{E,Si})_{grain,matrix}$ denotes the respective secondary ion intensities relative to Si shown in columns two and three.
[c] Si-normalized abundances (at.%) for the grain.
[d] err(+) and err(−) denote the positive and negative errors (all given errors are 1σ).

significantly enhanced, too, and we would expect a $^{26}Al/^{27}Al$-ratio 8–10 times higher than the calculated value. Y-grains originate from low-mass AGB stars of $Z \sim 1/2 \times Z_\odot$ (Amari et al., 2001), thus, the same case can be generally made here as for the Z-grains.

The parent stars of MS SiC grains, on the other hand, are low-mass ($M = 1.5$–3 $M_\odot$) AGB stars of about solar metallicity (e.g., Lugaro et al., 1999; Zinner et al., 2006) The stellar parent of KRY#I_37 would be compatible with the lower end of the mass range for the MS SiC sources. The Si-isotopic distribution of the MS SiC cannot be explained by the nucleosynthetic processes in their parent stars. Three different explanations are discussed for the observed spread: (i) Many AGB stars of different ages/-masses contributed SiC to the protosolar cloud; their initial Si isotopic ratios varied due to Galactic Chemical Evolution (e.g., Alexander and Nittler, 1999). (ii) The MS SiC parent stars formed in a relatively short time span, and the observed spread is due to local heterogeneities of the Si-isotopic composition in the ISM at the time of birth of these stars (e.g., Lugaro et al., 1999; Wasserburg et al., 2015). (iii) The merger of a low-Z satellite galaxy with the Milky Way $\sim$5–6 Gyr ago was the cause for the Si-isotopic range inferred for the stellar parents of the MS SiC grains (Clayton, 2003). From Fig. 5 it can be seen that the presolar silicates of Group 1 also show a comparably wide spread of their Si-isotopes, but it has to be kept in mind that many of the Si-isotopic compositions have considerably large error bars. A study of Si isotopes in presolar silicates by Vollmer et al. (2008) considered only grain data with errors <50‰; although the data set used there is much smaller than for presolar MS SiC grains, it seems to indicate a similar spread in their Si-isotopic compositions. For a direct comparison of the Si-isotopic composition of KRY#I_37 and MS SiC grains, it has to be taken into account that during the time of SiC formation, the Si-isotopic composition of the stellar envelope has been modified by TDU-mixing of s-processed Si. Vollmer et al. (2008) determined the isotopic shift for a 1.5 $M_\odot$-star of $\sim$solar metallicity to be $\Delta^{29}Si \cong +3‰$ and $\Delta^{30}Si \cong +17‰$; even with these modifications, the Si-isotopic composition of

our grain falls well within the range for MS SiC given in Zinner et al. (2006). Thus, the parent star of KRY#I_37 falls in the same mass range as the sources of mainstream SiC grains, which is in accordance with the stellar models from the F.R.U.I.T.Y. database that show the best agreement with the measured isotopic data. However, since the formation of SiC requires C/O > 1, the host star of the complex grain might not be identical with the SiC progenitor stars. Given the model-dependent uncertainties for metallicities and masses this is very well possible. Furthermore, we conclude that the Si isotopes of the grain studied here reflect essentially the initial composition of its parent star, in accordance with the argumentation by Lugaro et al. (1999) and Wasserburg et al. (2015).

4.2. Dust formation around O-rich stars and condensation sequence

In the following, we will explore if the core-mantle structure of grain KRY#I_37 truly resembles a condensation sequence. For a gas of photospheric composition (at $p^{tot} = 10^{-4}$ bar, Lodders (2003)) Al_2O_3 condenses first (at T = 1665 K), followed by hibonite ($CaAl_{12}O_{19}$), perovskite ($CaTiO_3$), Ca titanates with varying compositions (Ca_4Ti_3-O_{10}, $Ca_3Ti_2O_7$), and grossite ($CaAl_4O_7$). We consider all of these phases as potential components. However, to match the abundances obtained for the core region by AES (Table 3), it is necessary to add a Ti-rich, but Ca-poor component. Gail and Sedlmayr (1998) found that solid Ti compounds occur under low-pressure conditions as present in circumstellar envelopes ($p \leq 10^{-8}$ bar) at temperatures of $T \leq 1500$ K. From all the Ti-oxide species considered in the study by Gail and Sedlmayr (1998, 1999), TiO_2 is by far the most abundant type. In principle, $CaTiO_3$ (perovskite) is stable at slightly higher temperatures than TiO_2 in circumstellar envelopes (CSEs), but the formation of $CaTiO_3$-clusters is kinetically much less favorable than the homo-molecular formation of TiO_2-clusters (Gail and Sedlmayr, 1998, 1999).

If we include TiO_2 into our calculations, the composition of the inner part of KRY#I_37 (Table 3) can be

matched roughly by a mixture of 44% corundum, 48% TiO_2, 4.5% hibonite, and minor contributions of perovskite (3%) and grossite (0.5%). These components would equal a composition of 27 at.% Al, 2 at.% Ca, 10 at.% Ti and 62 at.% O, which fits the core composition determined by AES quite well (Table 3). However, one has to keep in mind that the numbers derived by AES bear some uncertainties, and it is beyond our calculations to provide a precise determination of individual phases in the core region of KRY#I_37. Nevertheless, it is an important finding that the elemental composition can be reproduced with Al_2O_3 and TiO_2 as major constituents, and only minor contributions from Ca-Ti- and Ca-Al-oxides.

Gail and Sedlmayr (1998, 1999) identified Al_2O_3 and TiO_2 as the first solid species forming from a cooling gas in the pressure range typical for circumstellar outflows (10^{-10} bar $\leq$ p $\leq 10^{-6}$ bar), with Al_2O_3 predicted to form via hetero-molecular condensation on seed nuclei, and solid TiO_2 by homo-molecular nucleation. Jeong et al. (2003) modeled the circumstellar envelope of the O-rich AGB star IRC –20197, for which molecular bands of TiO and VO had been reported. They found Al oxides and Ti oxides forming at ~2 stellar radii, with a mass fraction of Ti oxides of up to 30% in the grains, and silicate dust condensing at ~4.5 stellar radii. This Ti-oxide concentration corresponds quite well with our assumption for the composition of the inner part of KRY#I_37, as outlined above, since the 48 at.% of TiO_2 in the mixture equal a mass fraction of ~32 wt%.

After gehlenite, spinel ($MgAl_2O_4$) and anorthite ($CaAl_2Si_2O_8$) are the next mineral species to form, followed by forsterite (Mg_2SiO_4), diopside ($CaMgSi_2O_6$), and enstatite ($MgSiO_3$). From this sequence, one would expect the mantle to be gehlenite, spinel, or anorthite. However, the formation of gehlenite and spinel at even higher temperatures might have been prohibited locally, because the entire Al was already bound in other earlier formed minerals. Our results show that the silicate has a chemical composition largely compatible with diopside, and if we consider total pressures and dust/gas-ratios in the typical range for circumstellar envelopes (e.g., $p^{tot} \sim 10^{-6}$ to 10^{-8} bar (Jeong et al., 2003), and dust/gas $= 4 \times 10^{-3}$ to 9×10^{-2} (by mass) (Gobrecht et al., 2015)), we find that diopside condenses at higher temperatures than forsterite. If the accretion of the mantle did not occur by homogeneous condensation from the cooling gas, but by accretion of (very small) pre-existing clusters of varying compositions, this would potentially lead to a heterogeneous distribution of elements, as we see from the differing results from AES, EDS, and TOF-SIMS for the same sample regions. This is also documented by the heterogeneous distribution of Ca and Si (Fig. 6). As stated above, Fe appears to be anti-correlated with Ca and Si; thus, it may not be indigenous to the presolar grain. Instead, its presence might be due to residual matrix material in the grain area. Fine-grained Fe-rich matrix material could either be present in residual "pits" that reflect indentations in the grain's original surface, or might have been introduced into the grain by cracks in the grain's structure (an example for this is shown in Fig. 8 from Leitner et al., 2012).

As outlined above, the composition of grain KRY#I_37 corresponds well with a proposed formation of the grain around TiO_2 and Al_2O_3 condensation nuclei. However, only very few of the O-rich stardust grains found to date are actually complex grains. Moreover, Al-rich silicates are also rare, and no Ti-bearing presolar silicates have been found so far. This might either indicate that more than one condensation process is responsible for the formation of circumstellar dust, or that the seed nuclei are often too small, and the respective element concentrations too low, to be detected by most techniques applied for the study of these grains.

There are indeed several different models of grain nucleation in circumstellar dust shells. Gail and Sedlmayr (1998, 1999) and Gail (2003) propose Al- and Ti-(potentially together with Ca-) oxides as seed nuclei. Cluster formation of SiO as seed particles has been discussed by Gail et al. (2013), while Goumans and Bromley (2012) introduce a formation mechanism for Mg-rich, Fe-free silicates via hetero-molecular condensation based on Mg, SiO and H_2O. Finally, Goumans and Bromley (2013) show that silicate condensation can be started with the help of TiO_2, without the need for (macroscopic) TiO_2-cluster formation. Instead, one or a few TiO_2-molecules could be enough to initiate the dust condensation.

For KRY#I_37, we observed not only a significant amount of Ti in the core region, but also two Ti hotspots (Fig. 1), with approximate sizes of 300 nm × 460 nm (spot 1) and 270 nm × 715 nm (spot 2). We will now compare these sizes to the theoretical grain sizes from model calculations for dust formation and growth in CSEs. Typically, particle sizes in circumstellar growth zones are smaller than 1 μm (Gail, 2003), but from laboratory studies of a large number of presolar oxide grains, the existence of grains with sizes of up to several μm has been confirmed (e.g., Nittler et al., 1997, 2008). For a more specific estimate, we adopt the equation for the maximum possible radius for a particle in the outflow of an AGB star from Gail et al. (2009):

$$(4\pi/3)a_{max}^3 \varepsilon_d = (V_0 \varepsilon_{gr})/v_{gr} \text{ (their equation (31))}$$

with a_{max} being the maximum radius of the grain in the case of complete condensation of the condensable material. ε_d is the number of dust grains per H-nucleus, V_0 is the volume of the formula unit of the chemical compound in the solid, ε_{gr} is the abundance of the growth species relative to hydrogen, and v_{gr} represents the number of atoms of the key element in the formula of the solid. V_0 can be determined from

$$V_0 = A_d m_H / \rho_d$$

with A_d being the atomic weight of the chemical formula unit, m_H being the mass of the unified atomic mass unit, and ρ_d as the bulk density of the (macroscopic) condensate. With the parameters for TiO_2, we calculate $V_0 = (3.14–3.51) \times 10^{-23}$ cm^3 (depending on the crystal structure). $\varepsilon_{gr} = \varepsilon_{Ti} = 7.94 \times 10^{-8}$ if we assume a solar photospheric composition (Lodders et al., 2009), but bears an uncertainty of a factor of 10 (Gail et al., 2009), and ε_d varies from 10^{-14} to 10^{-11}, but usually has a value around 10^{-13} (Jeong et al., 2003). With $v_{gr} = 1$ (for TiO_2), we obtain an average a_{max}-

$\cong 0.02\ \mu m$, but with all uncertainties included, we find a range of $0.005\ \mu m \leq a_{max} \leq 0.2\ \mu m$. Thus, individual particles could well attain diameters of ~ 400 nm, which is also supported by the results from Jeong et al. (2003), showing that the mean particle size in the inner shell region can reach a value of $0.3\ \mu m$ or more. These estimated sizes are well compatible with the sizes of the Ti-spots in the central part of KRY#I_37, as well as the width of the whole core region ($\sim 0.3\ \mu m$). However, since the heterogeneous composition of the complex grain's core (Figs. 6 and 7) suggests that it formed by agglomeration of several subgrains, it might not even be necessary that the precursor grains reached the estimated maximum size.

A general issue that has to be considered in this context is the overall size of KRY#I_37. Typical average sizes for presolar silicate and oxide grains inferred from in situ studies are ~ 250 nm (e.g., Floss and Stadermann, 2009; Vollmer et al., 2009; Leitner et al., 2012). For presolar SiC, an average size of ~ 400 nm is observed, both for grain separates and in situ investigations by ion probe (Amari et al., 1994; Davidson et al., 2014). Does this observation imply that KRY#I_37 formed under highly unusual conditions? Albeit being among the largest O-rich presolar grains observed to date, it is not the only one found in this size range. The largest presolar silicate grains have sizes of $\sim 1\ \mu m$ (e.g., Nagashima et al., 2004), and some presolar oxides with sizes of several μm have been discovered in grain separates (e.g., Krestina and Hoppe, 2004; Bose et al., 2013). For SiC, even larger grains have been found, with diameters of up to 30 μm (e.g., Virag et al., 1992; Zinner et al., 2011). Amari et al. (1994) found that the size distributions of presolar SiC, graphite, and nanodiamonds all follow a log-normal distribution. They concluded this to be the preferred distribution law for grain formation in circumstellar envelopes, possibly reflecting a two-stage process of grain evolution by evaporation and recondensation. By exploring this log-normal distribution for SiC, we find that 3 μm-sized grains have a relative abundance (by number) of 3×10^{-4} compared to the 400 nm-sized fraction; for 6 μm-grains, the ratio decreases to $\sim 1 \times 10^{-5}$. If we apply the MRN model distribution (Mathis et al., 1977), where the abundance scales with $a^{-3.5}$ (a being the grain radius) to the presolar silicates and oxides, we estimate relative abundances of $\sim 8 \times 10^{-3}$ for 1 μm-sized grains and $\sim 3 \times 10^{-5}$ for 5 μm-sized grains relative to 250 nm-sized grains, which represent the average grain size. Even if we assume rather large uncertainties for this estimate, it is evident that the apparent "lack" of large grains in the O-rich presolar grain inventory is most likely due to the limited statistics (since < 1000 presolar silicate and oxide grains have been found by in situ ion imaging so far).

Ti-oxide stardust grains are very rare in our inventory of presolar grains and only a handful has been found to date (Nittler and Alexander, 1999; Nittler et al., 2008; Bose et al., 2010). Sizes for these grains are not well constrained, only Bose et al. (2010) report a size of 200×120 nm, while the other two studies only give the size ranges for the grain separate mounts that were investigated ($0.5\ \mu m < d < 5\ \mu m$, with the majority of the grains being smaller than 1.5 μm). In two studies, Ti-oxide subgrains were reported within

presolar Al-(Ca-) oxides (Leitner et al., 2012; Takigawa et al., 2014), with sizes of 100×80 nm and 40 nm, respectively. Zega et al. (2014) found several Ti-bearing subgrains with sizes < 100 nm in a presolar spinel grain from Orgueil, and Nguyen et al. (2014) reported traces of Ti in the spinel core of their complex grain. The presence of Ti was also confirmed by TEM-based EDS in one presolar Al_2O_3 grain (Stroud et al., 2004), another unusual Mg-rich Al-oxide grain (Stroud et al., 2007), and four presolar hibonite grains (Zega et al., 2011), but no evidence for subgrains was found. The study by Zega et al. (2011) provided Ti concentrations from 0.004 to 1.03 wt.% for 25 additional presolar Al_2O_3 and hibonite grains derived by SIMS, but no information on the distribution within the grains is available.

While several studies have been dedicated to the investigation of trace elements in presolar SiC grains (Amari et al., 1995; Henkel et al., 2007b; King et al., 2012), to our knowledge, no such investigations have been carried out on presolar O-rich grains. Our TOF-SIMS investigation confirmed the presence of V, Sr, and potentially Rb within KRY#I_37. As pointed out in the previous section, the derived abundances are calculated with the help of sensitivity factors, and expressed relative to a reference element. Commonly, Si is chosen as the reference element, but this only makes sense for the silicate mantle of KRY#I_37, since the core region is virtually Si-free.

As already pointed out earlier, due the spatial resolution of the TOF-SIMS-investigation, the element distributions could in principle be considered as homogeneous. However, Amari et al. (1995) reported a good correlation between the abundances of Ti and V in presolar SiC, and from Lodders (2003), we find that (for a gas of solar composition at $p^{tot} \sim 10^{-4}$ bar), both V and Sr condense into Ti-oxide, at similarly high temperatures ($T \sim 1429$ K and 1464 K, respectively), while Rb condenses at lower temperatures ($T \sim 800$ K) into silicate phases. Thus, it seems likely that V and Sr are present in the core, in association with Ti, while for Rb, a correlation with the silicate mantle appears more likely.

A comparison of the trace element data from this study with the results from investigations of SiC grains is not straightforward. Condensation of O-rich and C-rich circumstellar dust occurs in chemically different environments, and also at different stellar evolutionary stages, and both factors influence the availability and condensation behavior of a given (trace) element. Laboratory investigation of the trace element contents of presolar SiC (Amari et al., 1995), in combination with a theoretical treatment of the physical conditions determining their condensation (Lodders and Fegley, 1995), showed that the main factors determining trace element abundances are (1) the elemental composition of the gas from which the phase condenses, and (2) the condensation behavior under the prevalent physical conditions. Let us consider the elements Ti, V, and Sr, which should condense into the same host phase. If *all* of the available Ti, V, and Sr condensed into Ti-oxide seed particles, the V/Ti and Sr/Ti ratios should reflect the composition of the gas at the time of grain formation. The stellar model calculations from the F.R.U.I.T.Y. database are all based on CI-like initial compositions. At the

time of the FDU, no nucleosynthetic processing of the elements in question here has occurred, therefore, their respective ratios should still reflect the initial composition of the gas. For the V/Ti-ratio, we find that even after several TDU episodes, no significant deviation from CI is expected.

For Sr/Ti, a strong increase is predicted after the onset of TDU episodes. As can be seen from Fig. 9, both the V/Ti and Sr/Ti ratios for KRY#I_37 are below their respective CI values; this could be due to the higher volatility of V and Sr relative to Ti (Lodders, 2003). The physical and
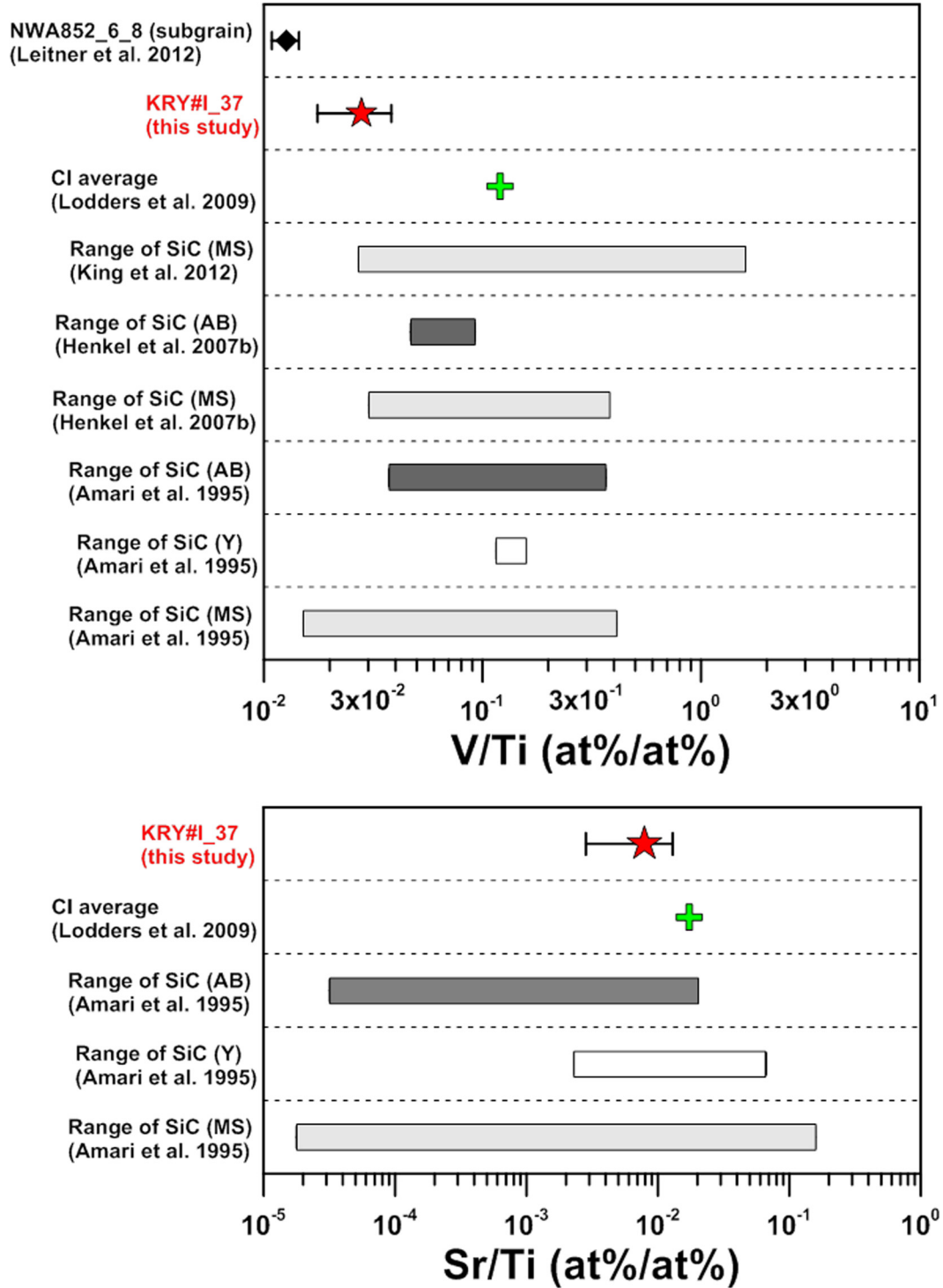

Fig. 9. V/Ti- and Sr/Ti abundance ratios determined for KRY#I_37, together with ratios recalculated from literature data for SiC grains from AGB stars (Amari et al., 1995; Henkel et al., 2007b; King et al., 2012), a Ti-oxide subgrain from a Group 1 presolar hibonite grain (Leitner et al., 2012), and the respective CI chondritic ratios (Lodders et al., 2009).

chemical processes involved in the nucleation of O-rich dust are even more complex than for SiC, thus, additional processes, like, e.g., condensation into different/competing dust species (with potentially differing condensational behaviors concerning the elements in question here), might well play a role which can clearly not be deduced from a single data point. However, we note that the V/Ti and Sr/Ti ratios lie within the ranges observed for SiC of AGB star origin. Moreover, the significantly lower V/Ti ratio observed for a Ti-rich subgrain from Leitner et al. (2012) (Fig. 9) indicates a certain range of values for O-rich presolar grains as well. Since it is clear for the SiC grains that their trace element contents are not dominantly influenced by stellar processes, but rather by condensational processes and the initial composition of the gas, we consider it valid to make the same assumption for O-rich grains.

It is well beyond the scope of this manuscript to unambiguously identify the most plausible nucleation mechanism (s) for oxides and silicates in stellar environments; this would require an extensive study with better detection limits than the ones typically achieved for EDS or AES studies (ranging from 0.1 to a few at.%). However, our study, as well as previous studies that reported Ti-oxide subgrains (Leitner et al., 2012; Takigawa et al., 2014; Zega et al., 2014) clearly demonstrates that Ti-oxides do indeed play a role in dust nucleation in some cases. The size of the seed particles may well be influenced by local concentrations of the molecular species; and if the mechanism proposed by Goumans and Bromley (2013) is correct (a few molecules are sufficient as condensation nuclei), Ti concentrations in many presolar silicates might simply be too low to be detected by most techniques.

Size and composition of the complex grain investigated here are highly unusual when compared to the vast majority of O-rich presolar grains. As we discussed earlier in this section, if we assume a log-normal size distribution for presolar O-rich dust, grains significantly larger than ~2 μm are expected to be rare in the current presolar grain inventory. The fact that dust formation around O-rich AGB stars is a rather complex process is confirmed by a multitude of observations from the CSEs of O-rich (Mira-type) AGB stars, and also by the detailed laboratory studies of presolar grains. The infrared (IR) spectra of these stars often show spectral bands characteristic for alumina (Al_2O_3) in the range from 9 μm to 15 μm, for silicates at about 9.7 μm and 18 μm, or a mixture of both features (e.g., Onaka et al., 1989; Speck et al., 2000; Molster and Waters, 2003). Karovicova et al. (2013) found in a high-resolution survey of four O-rich AGB stars that Al_2O_3 and silicate dust shells occurred together around the stars with the highest observed mass-loss rates. In addition, De Beck et al. (2015) reported recently for the first time the presence of TiO_2 dust around a red supergiant star.

Since the grain could not be prepared successfully by the focused ion beam (FIB) technique for transmission electron microscopy (TEM), we do not have any information on the crystal structure, i.e., it remains especially unclear if core and mantle are amorphous or crystalline.

Such structural information would have allowed further conclusions about the mass-loss rate of the parent star (Sogawa and Kozasa, 1999). However, there is room for some speculation. From Sogawa and Kozasa (1999, their Fig. 1), we see that the calculated radii for heterogeneous (core-mantle) grains, as well as the core radii, increase with increasing mass loss rates of the parent star (up to 200 nm for the highest mass loss rates considered there). The size of KRY#I_37 could thus be indicative of condensation around an AGB star with mass loss rate in the range of $\dot{M} \sim 10^{-4}$ $M_\odot yr^{-1}$, which would be among the maximum values determined for O-rich AGB stars ($\sim 10^{-7}$ $M_\odot yr^{-1}$ - $\leq \dot{M} \leq 10^{-4}$; e.g., Kastner, 1992; Loup et al., 1993). Formation of complex grains like KRY#I_37 might be correlated with the presence of multiple dust shells around their parent stars, as well as with the respective mass-loss rates. However, currently neither the available observational data set for O-rich AGB stars, nor the amount of complex presolar dust allow further conclusions. Moreover, the fact that the sizes for homogenous circumstellar grains predicted by the models are often far below the observed diameters for presolar grains indicates that the current theories for circumstellar dust formation need more refinement.

4.3. Observation of a phosphorus-bearing phase

We identified phosphorus in a sub-region of the complex grain by EDS and TOF-SIMS mapping (Figs. 7 and 8). Potential mass interferences in the TOF-SIMS spectra by $^{47}Ti^{16}O^-$ for $^{31}P^{16}O_2^-$ and by $^{47}Ti^{16}O_2^-$ for $^{31}P^{16}O_3^-$ can be ruled out, because no molecular peaks for $^{48}Ti^{16}O_n^-$ (the most abundant Ti-isotope) were observed, and the $^{31}P^{16}O_2^-$, $^{31}P^{16}O_3^-$-bearing spot was detected at the same position of the P-spot identified by EDS.

The question is whether the P-bearing subgrain is a primary phase inherited from the circumstellar envelope or a secondary phase that formed either in the ISM, the protosolar nebula, on the meteorite parent body, or by terrestrial weathering.

We observe no phosphorus reservoir in direct contact with the P-O-phase in KRY#I_37 (Figs. 7 and 8). No cracks or typical alteration products are visible near the grain, and we observe a sharp boundary between the P-bearing region and the adjacent matrix material. This does not completely rule out the introduction of P by aqueous alteration; however, it would have been necessary to introduce P, while retaining the anomalous oxygen from the grain in place. A second possibility is that P was added to the grain by implantation or chemical reactions in the ISM. Turner et al. (1990) observed that P is depleted in molecular cloud cores compared to the diffuse ISM, indicating that it is transferred by some mechanism from the gas phase into dust grains. Finally, the phosphorus could also have been inherited from circumstellar shell of the parent star; PN and PO molecules have been identified in the circumstellar envelope of at least one O-rich AGB star, IK Tauri (De Beck et al., 2013).

However, without structural and high-resolution chemical information on the P-bearing phase, its origin remains ambiguous, and, albeit unlikely (as discussed above), we cannot completely rule out that it is a matrix grain located "on top" of the respective region in the presolar grain.

5. SUMMARY AND CONCLUSIONS

We conducted a multi-isotope study in combination with a detailed investigation of the elemental composition of a complex O-rich presolar grain, consisting of an Al-Ca- Ti-oxide core, and a silicate mantle with a chemical composition largely compatible with diopside. Additionally, small amounts of V, Rb and Sr were found in the grain.

The O-isotopic composition of KRY#I_37 indicates an origin from a low-mass ($\sim$1.5 $M_\odot$) AGB star with a metallicity (Z) about 15% higher than the solar value. The presence of a small excess of radiogenic ^{26}Mg gives evidence for the occurrence of (now extinct) ^{26}Al, and together with the presence of small amounts of Rb and Sr in the grain and the observed O- and Ti-isotopic ratios, we can constrict condensation of the grain to a point early in the AGB-phase, at the onset of the third dredge-up episodes, but before larger amounts of nucleosynthetically processed material were mixed to the stellar surface. The Si-isotopic composition of the grain shows a small, but significant deviation from the Solar System value. In the context of the stellar properties inferred from the other isotopic systems that we studied, as well as the trace element composition, we conclude that the observed Si-isotopic composition represents the initial stellar composition and is not the result of nucleosynthetic processes within the parent star.

The sequence of chemical phases observed in KRY#I_37 resembles a condensation sequence from a cooling gas of solar composition at dust/gas-ratios and pressures characteristic for circumstellar envelopes of O-rich AGB stars. However, local conditions can well deviate from these simplified "ideal" assumptions, and processes like non-equilibrium chemistry induced by stellar pulsations (Gobrecht et al., 2015), perturbations that might create pressure gradients and variations in the dust/gas-ratio, grain-grain collisions and other stochastic processes (e.g., Brownian motion of the forming dust particles) can have an influence on dust formation. The heterogeneous composition of KRY#I_37 could well indicate a "clumping" of individual Ti- and (Ca-)Al-oxide particles, which then were transported outwards and accreted a mantle of silicate material, possibly again under the influence of local disturbances.

Our observations give evidence for grain condensation triggered by the presence of Ti- and Al-oxide nucleation seeds. By comparison with the (admittedly still limited) data set from high-resolution spectral investigations of O-rich AGB stars, the simultaneous occurrence of refractory oxide and silicate phases in grain KRY#I_37 might be indicative of a relatively high mass-loss rate of the parent star.

We report also the detection of a P-O-containing sub-grain; however, due to the loss of the sample during preparation for TEM analyses and the resulting lack of structural information for the grain, its origin remains ambiguous.

ACKNOWLEDGEMENTS

REFERENCES

Alexander C. M. O'D. and Nittler L. R. (1999) The galactic evolution of Si, Ti, and O isotopic ratios. *Astrophys. J.* **519**, 222–235.

Amari S., Lewis R. S. and Anders E. (1994) Interstellar grains in meteorites: I. Isolation of SiC, graphite, and diamond; size distributions of SiC and graphite. *Geochim. Cosmochim. Acta* **58**, 459–470.

Amari S., Hoppe P., Zinner E. and Lewis R. (1995) Trace element concentrations in single circumstellar silicon carbide grains from the Murchison meteorite. *Meteoritics* **30**, 679–693.

Amari S., Nittler L. R., Zinner E., Gallino R., Lugaro M. and Lewis R. S. (2001) Presolar SiC grains of Type Y: origin from low-metallicity asymptotic giant branch stars. *Astrophys. J.* **546**, 248–266.

Bland P. A., Stadermann F. J., Floss C., Rost D., Vicenzi E. P., Kearsley A. T. and Benedix G. K. (2007) A cornucopia of presolar and early solar system materials at the micrometer size range in primitive chondrite matrix. *Meteorit. Planet. Sci.* **42**, 1417–1427.

Boothroyd A. I. and Sackmann I.-J. (1999) The CNO isotopes: deep circulation in red giants and first and second dredge-up. *Astrophys. J.* **510**, 232–250.

Bose M., Floss C. and Stadermann F. (2010) An investigation into the origin of fe-rich presolar silicates in Acfer 094. *Astrophys. J.* **714**, 1624–1636.

Bose M., Floss C., Stadermann F., Stroud R. M. and Speck A. K. (2012) Circumstellar and interstellar material in the CO3 chondrite ALHA77307: An isotopic and elemental investigation. *Geochim. Cosmochim. Acta* **93**, 77–101.

Bose M., Zega T. J., Andronokov A. and Williams P. (2013) A large presolar oxide grain identified in allende CV3 chondrite. In *Lunar Planet. Sci. XLIV*. Lunar Planet. Inst., Houston, #3024 (abstr.).

Burbidge M. E., Burbidge G. R., Fowler W. A. and Hoyle F. (1957) Synthesis of the elements in stars. *Rev. Mod. Phys.* **29**, 547–650.

Busemann H., Nguyen A. N., Cody G. D., Hoppe P., Kilcoyne A. L. D., Stroud R. M., Zega T. J. and Nittler L. R. (2009) Ultra-primitive interplanetary dust particles from the comet 26P/Grigg–Skjellerup dust stream collection. *Earth Planet. Sci. Lett.* **288**, 44–57.

Cameron A. G. W. (1962) The formation of the sun and planets. *Icarus* **1**, 13–69.

Cameron A. G. W. (1973) Interstellar grains in museums? In *Interstellar Dust and Related Topics* (eds. J. M. Greenberg and H. C. van de Hulst). Reidel, Dordrecht, pp. 545–547.

Catanzaro E. J., Murphy T. J., Garner E. L. and Shields W. R. (1966) Absolute isotopic abundance ratios and the atomic weight of magnesium. *J. Res. NBS* **70A**, 453–458.

Choi B.-G., Huss G. R., Wasserburg G. J. and Gallino R. (1998) Presolar corundum and spinel in ordinary chondrites: origins from AGB stars and a supernova. *Science* **282**, 1284–1289.

Choi B.-G., Wasserburg G. J. and Huss G. R. (1999) Circumstellar hibonite and corundum and nucleosynthesis in asymptotic giant branch stars. *Astrophys. J.* **522**, L133–L136.

Clayton D. D. (2003) A presolar galactic merger spawned the SiC-grain mainstream. *Astrophys. J.* **598**, 313–324.

Cristallo S., Piersanti L., Straniero O., Gallino R., Domínguez I., Abia C., Di Rico G., Quintini M. and Bisterzo S. (2011) Evolution, nucleosynthesis, and yields of low-mass asymptotic giant branch stars at different metallicities. II. The FRUITY Database. *Astrophys. J. Suppl.* **197**, 17–27.

Davidson J., Busemann H. and Franchi I. A. (2012) A NanoSIMS and Raman spectroscopic comparison of interplanetary dust particles from comet Grigg-Skjellerup and non-Grigg Skjellerup collections. *Meteorit. Planet. Sci.* **47**, 1748–1771.

Davidson J., Busemann H., Nittler L. R., Alexander C. M. O'D., Orthous-Daunay F.-R., Franchi I. A. and Hoppe P. (2014) Abundances of presolar silicon carbide grains in primitive meteorites determined by NanoSIMS. *Geochim. Cosmochim. Acta* **139**, 248–266.

De Beck E., Kamiński T., Patel N. A., Young K. H., Gottlieb C. A., Menten K. M. and Decin L. (2013) PO and PN in the wind of the oxygen-rich AGB star IK Tauri. *Astron. Astrophys.* **558**, A132.

De Beck E., Vlemmings W., Muller S., Black J. H., O'Gorman E., Richards A. M. S., Baudry A., Maercker M., Decin L. and Humphreys E. M. (2015) ALMA observations of TiO_2 around VY Canis Majoris. *Astron. Astrophys.* **580**, A36.

Dwek E. (1998) The evolution of the elemental abundances in the gas and dust phases of the galaxy. *Astrophys. J.* **501**, 643–665.

El Eid M. F. (1994) CNO isotopes in red giants: theory versus observations. *Astron. Astrophys.* **285**, 915–928.

Floss C. and Stadermann F. J. (2009) Auger nanoprobe analysis of presolar ferromagnesian silicate grains from primitive CR chondrites QUE 99177 and MET 00426. *Geochim. Cosmochim. Acta* **73**, 2415–2440.

Floss C. and Stadermann F. J. (2012) Presolar silicate and oxide abundances and compositions in the ungrouped carbonaceous chondrite Adelaide and the K chondrite Kakangari: The effects of secondary processing. *Meteorit. Planet. Sci.* **47**, 992–1009.

Floss C. and Haenecour P. (2016) Presolar silicate grains: Abundances, isotopic and elemental compositions, and the effects of secondary processing. *Geochem. J.* **50**, 3–25.

Floss C., Stadermann F. J., Bradley J. P., Dai Z. R., Bajt S., Graham G. and Lea A. S. (2006) Identification of isotopically primitive interplanetary dust particles: A NanoSIMS isotopic imaging study. *Geochim. Cosmochim. Acta* **70**, 2371–2399.

Floss C., Stadermann F. J., Kearsley A. T., Burchell M. J. and Ong W. J. (2013) The abundance of presolar grains in Comet 81P/Wild 2. *Astrophys. J.* **763**, 140–150.

Gail H.-P. (2003) Formation and evolution of minerals in accretion disks and stellar outflows. In *Astromineralogy, Lecture Notes in Physics 609* (ed. T. Hennig). Springer, Heidelberg, pp. 55–120.

Gail H.-P. and Sedlmayr E. (1998) Inorganic dust formation in astrophysical environments. *Faraday Discuss.* **109**, 303–319.

Gail H.-P. and Sedlmayr E. (1999) Mineral formation in stellar winds: I. Condensation sequence of silicate and iron grains in stationary oxygen rich outflows. *Astron. Astrophys.* **347**, 594–616.

Gail H.-P., Zhukovska S. V., Hoppe P. and Trieloff M. (2009) Stardust from asymptotic giant branch stars. *Astrophys. J.* **698**, 1136–1154.

Gail H.-P., Wetzel S., Pucci A. and Tamanai A. (2013) Seed particle formation for silicate dust condensation by SiO nucleation. *Astron. Astrophys.* **555**, A119.

Gallino R., Arlandini C., Lugaro M., Busso M. and Straniero O. (1997) The New s-Process in Low Mass TP-AGB Stars. *Nucl. Phys. A* **621**, 423c–430c.

Gobrecht D., Cherchneff I. and Sarangi A. (2015) Dust formation in the inner wind of the oxygen-rich AGB Star IK Tau. In *ASP Conference Series 497* (eds. Kerschbaum, Wing and Hron). Astronomical Society of the Pacific, San Francisco, pp. 321–326.

Goumans T. P. M. and Bromley S. T. (2012) Efficient nucleation of stardust silicates via heteromolecular homogeneous condensation. *Mon. Not. R. Astron. Soc.* **420**, 3344–3349.

Goumans T. P. M. and Bromley S. T. (2013) Stardust silicate nucleation kick-started by $SiO + TiO_2$. *Philos. Trans. Roy. Soc. A* **371**, 20110580.

Henkel T., Tizard J., Blagburn D. and Lyon I. (2006) Interstellar dust laser explorer (IDLE): A new instrument for submicron analyses of stardust-quantification of laser SNMS. *Appl. Surf. Sci.* **252**, 7117–7119.

Henkel T., Tizard J., Blagburn D. and Lyon I. (2007a) Interstellar dust laser explorer: A new instrument for elemental and isotopic analysis and imaging of interstellar and interplanetary dust. *Rev. Sci. Instrum.* **78**, 055107.

Henkel T., Stephan T., Jessberger E. K., Hoppe P., Strebel R., Amari S. and Lewis R. S. (2007b) 3-D elemental and isotopic composition of presolar silicon carbides. *Meteorit. Planet. Sci.* **42**, 1121–1134.

Hillion F., Kilburn M. R., Hoppe P., Messenger S. and Weber P. K. (2008) The effect of QSA on S, C, O and Si isotopic ratio measurements. *Geochim. Cosmochim. Acta* **73**, A377.

Hoppe P., Annen P., Strebel R., Eberhardt P., Gallino R., Lugaro M., Amari S. and Lewis R. S. (1997) Meteoritic silicon carbide grains with unusual Si-isotopic compositions: evidence for an origin in low-mass, low-metallicity asymptotic giant branch stars. *Astrophys. J.* **487**, L101–L104.

Hoppe P., Leitner J., Gröner E., Marhas K. K., Meyer B. and Amari S. (2010) NanoSIMS studies of small presolar SiC grains: New insights into supernova nucleosynthesis, chemistry, and dust formation. *Astrophys. J.* **719**, 1370–1384.

Hoppe P., Leitner J. and Kodólanyí J. (2015) New constraints on the abundances of silicate and oxide stardust from supernovae in the Acfer 094 meteorite. *Astrophys. J.* **808**, L9–L14.

Huss G. R., Fahey A. J., Gallino R. and Wasserburg G. J. (1994) Oxygen isotopes in circumstellar Al_2O_3 grains from meteorites and stellar nucleosynthesis. *Astrophys. J.* **430**, L81–L84.

Hutcheon I. D., Huss G. R., Fahey A. J. and Wasserburg G. J. (1994) Extreme ^{26}Mg and ^{17}O enrichments in an orgueil corundum: identification of a presolar oxide grain. *Astrophys. J.* **425**, L97–L100.

Jeong K. S., Winters J. M., Le Bertre T. and Sedlmayr E. (2003) Self-consistent modeling of the outflow from the O-rich Mira IRC –20197. *Astron. Astrophys.* **407**, 191–206.

Jones A. P., Tielens A. G. G. M. and Hollenbach D. J. (1996) Grain shattering in shocks: the interstellar grain size distribution. *Astrophys. J.* **469**, 740–764.

Karovicova I., Wittkowski M., Ohnaka K., Boboltz D. A., Fossat E. and Scholtz M. (2013) New insights into the dust formation of oxygen-rich AGB stars. *Astron. Astrophys.* **560**, A75.

Kastner J. H. (1992) Mass-loss rates for IRAS-bright red giants: A revised model of circumstellar CO emission. *Astrophys. J.* **401**, 337–352.

King A., Henkel T., Rost D. and Lyon I. (2010) Determination of relative sensitivity factors during secondary ion sputtering of silicate glasses by Au^+, Au_2^+ and Au_3^+ ions. *Rapid Commun. Mass Spectrom.* **24**, 15–20.

King A. J., Henkel T., Rost D. and Lyon I. C. (2012) Trace element depth profiles in presolar silicon carbide grains. *Meteorit. Planet. Sci.* **47**, 1624–1643.

Kobayashi C., Karakas A. I. and Umeda H. (2011) The evolution of isotope ratios in the Milky Way Galaxy. *Mon. Not. R. Astron. Soc.* **414**, 3231–3250.

Kodólanyí J., Hoppe P., Gröner E., Pauly C. and Mücklich F. (2014) The Mg isotope composition of presolar silicate grains from red giant stars. *Geochim. Cosmochim. Acta* **140**, 577–605.

Krestina N., Hsu W. and Wasserburg G. J. (2002) Circumstellar oxide grains in ordinary chondrites and their origin. In *Lunar Planet. Sci. XXXIII*. Lunar Planet. Inst., Houston, #1425 (abstr.).

Krestina N. and Hoppe P. (2004) A NanoSIMS study of two new presolar spinel grains from the bishunpur ordinary chondrite. In *Lunar Planet. Sci. XXXV*. Lunar Planet. Inst., Houston, #1670 (abstr.).

Lattanzio J. C. and Boothroyd A. I. (1997) Nucleosynthesis of elements in low to intermediate mass stars through the AGB phase. *AIP Conf. Proc.* **402**, 85–114.

Leitner J., Hoppe P. and Heck P. R. (2010) First discovery of presolar material of possible supernova origin in impact residues from comet 81P/Wild 2. In *Lunar Planet. Sci. XLI*. Lunar Planet. Inst., Houston, #1607 (abstr.).

Leitner J., Vollmer C., Hoppe P. and Zipfel J. (2012) Characterization of presolar material in the CR chondrite northwest Africa 852. *Astrophys. J.* **745**, 38–53.

Leitner J., Metzler K. and Hoppe P. (2014) Characterization of Presolar Grains In Cluster Chondrite Clasts from Unequilibrated Ordinary Chondrites. In *Lunar Planet. Sci. XLV*. Lunar Planet. Inst., Houston, #1099 (abstr.).

Leitner J., Hoppe P., Floss C., Hillion F. and Henkel T. (2016) Correlated nanoscale study of a unique complex stardust grain. *Meteorit. Planet. Sci.* **51**, A404.

Lodders K. (2003) Solar system abundances and condensation temperatures of the elements. *Astrophys. J.* **591**, 1220–1247.

Lodders K. and Fegley, Jr., B. (1995) The origin of circumstellar silicon carbide grains found in meteorites. *Meteoritics* **30**, 661–678.

Lodders K. and Amari S. (2005) Presolar grains from meteorites: Remnants from the early times of the solar system. *Chem. Erde* **65**, 93–166.

Lodders K., Palme H. and Gail H.-P. (2009). *Abundances of the Elements in the Solar System*. , arXiv:0901.1149.

Loup C., Foreville T., Omont A. and Paul J. F. (1993) CO and HCN observations of circumstellar envelopes. A catalogue – mass loss rates and distributions. *Astron. Astrophys., Suppl. Ser.* **99**, 291–377.

Lugaro M., Zinner E., Gallino R. and Amari S. (1999) Si isotopic ratios in mainstream presolar SiC grains revisited. *Astrophys. J.* **527**, 369–394.

Lugaro M., Karakas A. I., Bruno C. G., Aliotta M. and Nittler L. R., et al. (2017) Origin of meteoritic stardust unveiled by a revised proton-capture rate of ^{17}O. *Nat. Astron.* **1**, 0027.

Mathis J. S., Rumpl W. and Nordsieck K. H. (1977) The size distribution of interstellar grains. *Astrophys. J.* **217**, 425–433.

Messenger S., Keller L. P., Stadermann F. J., Walker R. M. and Zinner E. (2003) Samples of stars beyond the solar system: silicate grains in interplanetary dust. *Science* **300**, 105–108.

Metzler K. (2012) Ultrarapid chondrite formation by hot chondrule accretion? Evidence from unequilibrated ordinary chondrites. *Meteorit. Planet. Sci.* **47**, 2193–2217.

Molster F. J. and Waters L. B. F. M. (2003) The mineralogy of interstellar and circumstellar dust. In *Astromineralogy, Lecture Notes in Physics 609* (ed. T. Hennig). Springer, Heidelberg, pp. 121–170.

Mostefaoui S. and Hoppe P. (2004) Discovery of abundant in situ silicate and spinel grains from red giant stars in a primitive meteorite. *Astrophys. J.* **613**, L149–L152.

Nagashima K., Krot A. N. and Yurimoto H. (2004) Stardust silicates from primitive meteorites. *Nature* **428**, 921–924.

Nguyen A. N. and Zinner E. (2004) Discovery of ancient silicate stardust in a meteorite. *Science* **303**, 1496–1499.

Nguyen A. N. and Messenger S. (2014) Resolving the stellar sources of isotopically rare presolar silicate grains through Mg and Fe isotopic analyses. *Astrophys. J.* **784**, 149–163.

Nguyen A. N., Stadermann F. J., Zinner E., Stroud R. M., Alexander C. M. O'D. and Nittler L. R. (2007) Characterization of presolar silicate and oxide grains in primitive carbonaceous chondrites. *Astrophys. J.* **656**, 1223–1240.

Nguyen A. N., Nittler L. R., Stadermann F. J., Stroud R. M. and Alexander C. M. O'D. (2010) Coordinated analyses of presolar grains in the Allan Hills 77307 and Queen Elizabeth Range 99177 Meteorites. *Astrophys. J.* **719**, 166–189.

Nguyen A. N., Nakamura-Messenger K., Messenger S., Keller L. P. and Klöck W. (2014) Identification of a compound spinel and silicate presolar grain in a chondritic interplanetary dust particle. In *Lunar Planet. Sci. XLV*. Lunar Planet. Inst., Houston, #2351 (abstr.).

Nittler L. R. (2009) On the mass and metallicity distributions of the parent AGB stars of O-Rich presolar stardust grains. *Publ. Astron. Soc. Aust.* **26**, 271–277.

Nittler L. R. and Alexander C. M. O'D. (1999) Automatic identification of presolar Al- and Ti-rich oxide grains from ordinary chondrites. In *Lunar Planet. Sci. XXX*. Lunar Planet. Inst., Houston, #2041 (abstr.).

Nittler L. R., Alexander C. M. O'D., Gao X., Walker R. M. and Zinner E. K. (1994) Interstellar oxide grains from the Tieschitz ordinary chondrite. *Nature* **370**, 443–446.

Nittler L. R., Alexander C. M. O'D., Gao X., Walker R. M. and Zinner E. (1997) Stellar sapphires: the properties and origins of presolar Al_2O_3 in meteorites. *Astrophys. J.* **483**, 475–495.

Nittler L. R., Alexander C. M. O'D., Stadermann F. J. and Zinner E. K. (2005) Presolar Al-, Ca-, and Ti-rich Oxide Grains in the Krymka Meteorite. In *Lunar Planet. Sci. XXXVI*. Lunar Planet. Inst., Houston, #2200 (abstr.).

Nittler L. R., Alexander C. M. O'D., Gallino R., Hoppe P., Nguyen A. N., Stadermann F. J. and Zinner E. K. (2008) Aluminum-, calcium- and titanium-rich oxide stardust in ordinary chondrite meteorites. *Astrophys. J.* **682**, 1450–1478.

Nittler L. R., Alexander C. M. O'D. and Stroud R. M. (2013) High abundance of presolar materials in CO3 chondrite dominion Range 08006. In *Lunar Planet. Sci. XLIV*. Lunar Planet. Inst., Houston, #2367 (abstr.).

Nollett K. M., Busso M. and Wasserburg G. J. (2003) Cool bottom processes on the thermally pulsing asymptotic giant branch and the isotopic composition of circumstellar dust grains. *Astrophys. J.* **582**, 1036–1058.

Onaka T., de Jong T. and Willems F. J. (1989) A study of M Mira variables based on IRAS LRS observations. I. Dust formation in the circumstellar shell. *Astron. Astrophys.* **218**, 169–179.

Palmerini S., La Cognata M., Cristallo S. and Busso M. (2011) Deep mixing in evolved stars. I. The effect of reaction rate revisions from C to Al. *Astrophys. J.* **729**, 3–23.

Slodzian G., Hillion F., Stadermann F. J. and Zinner E. (2004) QSA influences on isotopic ratio measurements. *Appl. Surf. Sci.* **231–232**, 874–877.

Sogawa H. and Kozasa T. (1999) On the origin of crystalline silicate in circumstellar envelopes of oxygen-rich asymptotic giant branch stars. *Astrophys. J.* **516**, L33–L36.

Speck A. K., Barlow M. J., Sylvester R. J. and Hofmeister A. M. (2000) Dust features in the 10-μm infrared spectra of oxygen-rich evolved stars. *Astron. Astrophys., Suppl. Ser.* **146**, 437–464.

Stadermann F. J., Floss C. and Wopenka B. (2006) Circumstellar aluminum oxide and silicon carbide in interplanetary dust particles. *Geochim. Cosmochim. Acta* **70**, 6168–6179.

Stadermann F. J., Hoppe P., Floss C., Heck P. R., Hörz F., Huth J., Kearsley A. T., Leitner J., Marhas K. K., McKeegan K. D. and Stephan T. (2008) Stardust in stardust-the C, N, and O isotopic compositions of Wild 2 cometary matter in Al foil impacts. *Meteorit. Planet. Sci.* **43**, 299–313.

Stadermann F. J., Floss C., Bose M. and Lea A. S. (2009) The use of Auger spectroscopy for the in situ elemental characterization of sub-micrometer presolar grains. *Meteorit. Planet. Sci.* **44**, 1033–1049.

Stephan T. (2001) TOF-SIMS in cosmochemistry. *Planet. Space Sci.* **49**, 859–906.

Strebel R., Hoppe P. and Eberhardt P. (1997) Nitrogen, oxygen, magnesium, and titanium isotopic compositions of circumstellar oxide grains from the tieschitz and orgueil meteorites. *Meteorit. Planet. Sci.* **32**, A125.

Stroud R. M., Nittler L. R. and Alexander C. M. O'D. (2004) Polymorphism in presolar Al$_2$O$_3$ grains from asymptotic giant branch stars. *Science* **305**, 1455–1457.

Stroud R. M., Nittler L. R., Alexander C. M. O'D. and Zinner E. (2007) Transmission electron microscopy and secondary ion mass spectrometry of an unusual Mg-rich presolar Al2O3 grain. In *Lunar Planet. Sci. XXXVIII*. Lunar Planet. Inst., Houston, #2203 (abstr.).

Takigawa A., Stroud R. M., Nittler L. R. and Alexander C. M. O'D. (2014) A titanium oxide grain within a presolar corundum. *Meteorit. Planet. Sci.* **49**, A390.

Timmes F. X., Woosley S. E. and Weaver T. A. (1995) Galactic chemical evolution: hydrogen through zinc. *Astrophys. J. Suppl.* **98**, 617–658.

Tonotani A., Kobayashi S., Nagashima K., Sakamoto N., Russell S. S., Itoh S. and Yurimoto H. (2006) Presolar grains from primitive ordinary chondrites. In *Lunar Planet. Sci. XXXVII*. Lunar Planet. Inst., Houston, #1539 (abstr.).

Turner B. E., Tsuji T., Bally J., Guelin M. and Cernicharo J. (1990) Phosphorus in the dense interstellar medium. *Astrophys. J.* **365**, 569–585.

Virag, A., Wopenka, B., Amari, S., Zinner, E., Anders, E., Lewis, R. S. (1992) .Isotopic, optical, and trace element properties of large single SiC grains from the Murchison meteorite.

Vollmer C., Hoppe P., Brenker F. E. and Palme H. (2006) A complex presolar grain in Acfer 094 – Fingerprints of a Circumstellar Condensation Sequence? In *Lunar Planet. Sci. XXXVII*. Lunar Planet. Inst., Houston, #1284 (abstr.).

Vollmer C., Hoppe P. and Brenker F. (2008) Si isotopic compositions of presolar silicate grains from red giant stars and supernovae. *Astrophys. J.* **684**, 611–617.

Vollmer C., Hoppe P., Stadermann F. J., Floss C. and Brenker F. (2009) NanoSIMS analysis and Auger electron spectroscopy of silicate and oxide stardust from the carbonaceous chondrite Acfer 094. *Geochim. Cosmochim. Acta* **73**, 7127–7149.

Wasserburg G. J., Trippella O. and Busso M. (2015) Isotope anomalies in the Fe-group elements in meteorites and connections to nucleosynthesis in AGB stars. *Astrophys. J.* **805**, 7–24.

Woitke P., Dominik C. and Sedlmayr E. (1993) Dust destruction in the transition region between stellar wind and interstellar medium. *Astron. Astrophys.* **274**, 451–464.

Zega T. J., Alexander C. M. O'D., Nittler L. and Stroud R. M. (2011) A transmission electron microscopy study of presolar hibonite. *Astrophys. J.* **730**, 83–92.

Zega T. J., Nittler L. R., Gyngard F., Alexander C. M. O'D., Stroud R. M. and Zinner E. K. (2014) A transmission electron microscopy study of presolar spinel. *Geochim. Cosmochim. Acta* **124**, 152–169.

Zhao X., Floss C., Lin Y. and Bose M. (2013) Stardust investigation into the CR chondrite grove mountain 021710. *Astrophys. J.* **769**, 49–64.

Zinner E. (2014) Presolar Grains. In *Meteorites and Cosmochemical Processes* (ed. A. M. Davis). Elsevier, Amsterdam, pp. 181–213.

Zinner E., Amari S., Guinness R., Nguyen A., Stadermann F. J., Walker R. M. and Lewis R. S. (2003) Presolar spinel grains from the Murray and Murchison carbonaceous chondrites. *Geochim. Cosmochim. Acta* **67**, 5083–5095.

Zinner E., Nittler L. R., Hoppe P., Gallino R., Straniero O. and Alexander C. M. O'D. (2005) Oxygen, magnesium and chromium isotopic ratios of presolar spinel grains. *Geochim. Cosmochim. Acta* **69**, 4149–4165.

Zinner E., Nittler L. R., Gallino R., Karakas A. I., Lugaro M., Straniero O. and Lattanzio J. C. (2006) Silicon and carbon isotopic ratios in AGB Stars: SiC grain data, models, and the galactic evolution of the Si isotopes. *Astrophys. J.* **650**, 350–373.

Zinner E., Jadhav M., Gyngard F. and Nittler L. R. (2011) Bonanza, a huge presolar SiC grain of type X. In *Lunar Planet. Sci. XLII*. Lunar Planet. Inst., Houston, #1070 (abstr.).

Associate editor: Anders Meibom